Shape, functionnalisation and defects effects on theranostic anisotropic nano-objects coated with antifouling dendrons

SCHOLARONE™
Manuscripts

Shape, functionnalisation and defects effects on theranostic anisotropic nano-objects coated with antifouling dendrons

Geoffrey Cotin[1], Cristina Blanco-Andujar[1], Francis Perton[1], Laura Asín[2], Jesus M. de la Fuente[2], Wilfried Reichardt[3,4,5], Denise Schaffner[3], Dinh-Vu Ngyen[1], Damien Mertz[1], Céline Kiefer, Benoit P. Pichon[1], Florent Meyer[6], Simo Spassov[7], Ovidiu Ersen[1], Michael Chatzidakis[8], Gianluigi A. Botton[8], Céline Hénoumont[9], Sophie Laurent[9], Jean-Marc Greneche, Delphine Felder-Flesch[1], Franscisco J. Teran[11,12], Daniel Ortega[11], Sylvie Begin-Colin[1,*]

[1] Université de Strasbourg, CNRS, Institut de Physique et Chimie des Matériaux de Strasbourg, UMR 7504, F-67034 Strasbourg, France

[2] Instituto de Ciencia de Materiales de Aragón, ICMA. CSIC-University of Zaragoza & CIBER-BBN, 50018 Zaragoza, Spain

[3] Department of Radiology, Medical Physics, Medical Center, University of Freiburg, Faculty of Medicine, University of Freiburg, Germany

[4] German Cancer Consortium (DKTK), Heidelberg, Germany

[5] German Cancer Research Center (DKFZ), Heidelberg, Germany

[6] Université de Strasbourg, INSERM, UMR 1121 Biomaterials and Bioengineering, FMTS, F-67000 Strasbourg, France

[7] Centre de Physique du Globe de l'Institut Royal Météorologique de Belgique

[8] Dept of Materials Science and Engineering, McMaster University, 1280 Main Street West, Hamil-ton, Ontario, Canada, L8S 4M1

[9] Université de Mons, General, Organic and Biomedical Chemistry Unit, NMR and Molecular Imag-ing Laboratory, 7000 Mons, Belgium

[10] Institut des Molécules et Matériaux du Mans IMMM UMR CNRS 6283, Université du Maine, Avenue Olivier Messiaen, 72085 Le Mans Cedex 9, France

[11] iMdea Nanociencia, Campus Universitario de Cantoblanco, 28049 Madrid, Spain

[12] Nanobiotecnología (iMdea-Nanociencia), Unidad Asociada al Centro Nacional de Biotecnología (CSIC), 28049 Madrid, Spain

ABSTRACT: Among the virtues of nanomedicine theranostic agents, it is the stealthiness to evade the reticulo-endothelial system and a good biodistribution to enable specific diseases targeting and an image-guided therapy. Here, biocompatible iron-oxide nanoparticles with different shapes (spherical, plate, cubic, octopod) were designed and screened in vitro and in vivo to evaluate their abilities as high-end theranostic agents. Octopods coated with dendron molecules showed an unprecedented combination of characteristics as image contrast and magnetic hyperthermia agents especially at low frequency. Besides octopods, nanospheres with size around 20 nm also revealed interesting combined theranostic properties. The dendron coating provides anti-fouling properties and small hydrodynamic size favoring an in vivo circulation. The extensive structural and magnetic characterization of dendronized nanoparticles evidences a clear shape and defect effect affecting their performance. Octopod and nanoplate shapes appeared to induce unusual surface effects demonstrated by Electron Energy Loss and Mossbauer spectroscopies whereas nanospheres were shown to display high internal defects favoring Neel relaxation for magnetic hyperthermia. All measurements evidenced a particular signature of octopods which is attributed to higher anisotropy, surface effects and/or magnetic field inhomogeneity induced by tips. Neel relaxation is favored at sizes lower than 20 nm when the brownian ones occurs at higher size.

1. Introduction

In the field of the synthesis and functionalization of iron oxide nanoparticles (NPs) for biomedical applications, most researches aim at developing multifunctional theranostic NPs which can both identify disease states and deliver locally therapy, thus allowing monitoring therapy by imaging[1–6]. The current challenge in iron oxide-based NPs engineering is thus to improve their design to allow combining in one nano-formulation both therapy by magnetic hyperthermia (MH) and imaging as contrast agent with the best efficiency in order to reduce the dose injected to the patient.

Superparamagnetic iron oxide NPs (IONPs) have already been commercially used as T2 contrast agent for MRI[7] and are of particular interest as biodegradable and non-toxic nano-objects compared to other contrast agents families[8,9]. The higher their magnetization saturation (Ms) value, the better the contrast. Yet this value is not only dependent on the NP structure but also on its aggregation state and the ability of water molecules to diffuse through the organic coating close to the magnetic core[7,8].

IONPs are also developed for magnetic hyperthermia (MH). When exposed to alternating magnetic fields (AMF) of appropriate intensity and frequency, these NPs release heat locally (where they are concentrated), which reduces the viability of cancer cells. The use of MH as a stand-alone or adjunct therapy for cancer is closer to a wider clinical implementation thanks to the positive results from the seminal clinical trials carried out by MagforceTM(Germany)[7,10–12], a nanomedicine company that succeeded in securing a 35 €M loan of the European Investment bank to further roll-out their therapy across Europe[13]. Nonetheless, there is currently a need of improving the available nanomaterials for MH to, for example, reduce the injected dose, better address difficult tumour locations or to lower the frequency and/or intensity of the applied field. Different parameters may be varied to increase the effective heat loss of iron oxide NPs such as their size, shape and/or composition among others. Indeed the amount of heat generated by NPs is highly dependent on the NPs structural and magnetic properties, and first studies have shown that spherical iron oxide NPs with a mean size around 20 nm are suitable for clinical MH[8,9]. More precisely, for frequencies and magnetic field amplitudes used in MH, prior studies carried out using field conditions where $H*f < 5 \times 10^9$ $Am^{-1}s^{-1}$ suggested an optimal diameter of 14 nm for standard spherical NPs. However given the variation in the anisotropy of different synthesized magnetite ($Fe_{3-x}O_4$) NPs (of similar size), the experimental optimal diameter appeared to fall between a broad range between 12 and 20 nm[9,14,15]. Indeed the magnetic properties of iron oxide NPs strongly depend on the synthesis method,[16–18] while heating values, such as Specific Adsorption Rate (SAR) ones, depend strongly on the measurement parameters (field frequency and amplitude, viscosity, NPs concentration) which strongly vary from one paper to another[8].

Besides changing nanoparticle size is limited as the superparamagnetic behavior will disappear above a specific size leading to suspensions with a colloidal stability affected by magnetic interactions. To circumscribe this problem, other options to improve their NP heating capabilities, are for example to change either its shape or its composition. Among the highest SAR values reported on NPs with different shapes, one may cite Guardia et al[19] who showed that cubic iron oxide NPs with a mean size of 19 nm presented tremendous heating power as well as Lartigue et al.[20] who developed nanoflowers consisting of aggregates of nanocrystals sharing common crystallographic planes. High relaxivity and SAR values have also been reported for octopod shaped NPs[21,22]. Alternatively, doping with Mn or Co[14,15,23] was also found to increase heating power. Recently, Pellegrino et al. boosted the heating power of the cubic NPs by doping with cobalt[24]. Synthesis of other shapes was also reported as for example nanoplates[25,26] or nanotubes[27]. Indeed, a lot of progress have been made in synthesis methods of NPs, revealing the thermal decomposition method as one of the most – if not the most – versatile one to tailor nanoparticle shape, as exemplified by the so produced nanocubes[28–30], spherical NPs with different sizes[31] and also octopods[21,22,32]. However, no clear trends have been established on which parameters are mostly responsible for influencing theranostic properties[8].

Another key point is the design of the organic coating[33] which is also challenging due to the multiple purpose organic coating must serve. Indeed, the molecules anchored to the surface of NPs may add different functions, such as dyes for optical imaging, targeting ligands to reach the target tissue or cells, or therapeutic agents (drug delivery). Other desirable functions include preventing NPs from agglomeration in a physiological environment and favoring their biodistribution and bioelimination (preventing opsonization of NPs and increasing their ability to evade the reticulo-endothelial system (RES)). Besides polymers, which have been widely studied up to now, another class of molecule is emerging, i.e small dendrons[34–37]. Bifunctional dendrons are promising as the diversity of functionalization brought by the arborescent structure simultaneously responded to the need for biocompatibility, low toxicity, large in vivo stability and specificity. The grafting of dendrons on the surface of 10 nm iron oxide NPs using phosphonate group as coupling agent has led to a new generation of MRI contrast agents (CA). These nano-objects show relaxivity values higher than those of commercial CAs combined to a very favorable biodistribution in mice without a significant uptake in healthy tissues and in particular liver (good bioelimination)[18,38–40]. The use of such dendrons appeared as a good way to ensure, after the grafting step, a mean hydrodynamic particle size below 100 nm together with a narrow size distribution in suspension, both being prerequisites for a good biodistribution, i.e avoiding RES uptake.

In this work, spherical, cubic, octopod and plate –shaped NPs whose synthesis optimization is detailed in reference[25] are coated with small dendron molecules and their in vitro and in vivo theranostic properties are investigated and correlated to their microstructural, surface and magnetic signatures. Their magnetic properties have been investigated in depth and correlated to their properties as contrast agent for MRI and heating agent for magnetic hyperthermia.

2. Experimental conditions

Synthesis of iron stearate precursor: Iron stearate (II) named hereafter $FeSt_2$ and (III) named hereafter $FeSt_3$ were prepared by precipitation of sodium stearate and ferrous chloride or ferric chloride salts in an aqueous solution, respectively as previously reported[25]. Briefly, sodium stearate (9.8 g, 32 mmol) was transferred into a 2-necked round bottomed flask (RBF) and solubilized in distilled H_2O (dH2O, 320 ml). The solution was heated to reflux and stirred for 30 min until complete dissolution of the stearate. Separately, $FeCl_2.4H_2O$ (3.16 g, 16 mmol) or $FeCl_3.6H_2O$ (2,88 g, 16 mmol) was dissolved in dH2O (160 ml) and added onto the sodium stearate solution under vigorous stirring. A light orange precipitate was formed immediately. The solution was kept under stirring conditions at this temperature for 15 min. Thereafter, the solution was allowed to cool down to room temperature (RT). The obtained precipitate was washed once by centrifugation (hot dH2O, 14000 rpm, 10 min). The product was then filtrated with a büchner funnel and oven dried at 65 °C for 24 h.

Synthesis of spheres. Iron oxide nanospheres (NS) were synthesized by thermal decomposition of an iron stearate precursor in the presence of oleic acid (OA) in an organic solvent. For the synthesis of NPs with a mean size around 20 nm: $FeSt_3$ (1.85 g, 2 mmol) was mixed with OA (1.89 g, 6.7 mmol) in squalane (15.8 g, 19.5 ml) and dibenzylether (DBE, 0.53 g, 0.5 ml) in a two neck RBF. The mixture was heated under stirring to 120 °C and kept at this temperature for 60 min without reflux condenser in order to dissolve the reactants and remove water residues. The condenser was then connected to the flask and the solution heated to 330 °C (5 °C/min) and kept under reflux for 60 min under air. After cooling to RT, a black and viscous suspension was obtained which was solubilized in chloroform (10 ml). The NPs were precipitated by addition of an excess of acetone and washed three times with chloroform and acetone at a ratio of 1:4 at 14000 rpm for 5 min by centrifugation. The NPs were resuspended in THF (50 ml) and stored until further use.

Synthesis of nanocubes. Iron oxide nanocubes (NC) were synthesized from iron stearate (III). $FeSt_3$ (2.72 g, 3 mmol) was mixed with OA (0.45 g, 1.5 mmol) and NaOl (0.45 g, 1.6 mmol) in eicosene (15 ml) in a two neck-RBF. The mixture was heated to 120 °C under stirring and kept at this temperature for 30 min without reflux condenser in order to dissolve the reactants and remove the water residues. The condenser was then connected to the flask and the solution heated to boiling temperature ($\approx$343 °C, 15 °C/min). The solution was kept at reflux for 90 min under air. After cooling to RT, a black gel was obtained. The NPs were washed as previously described.

Synthesis of nanoplates. Iron oxide nanoplates (NPl) were synthesized from iron stearate (II). $FeSt_2$ (1.44 g, 2.3 mmol) was mixed with OA (0.18 g, 0.65 mmol) and NaOl (0.70 g, 2.30 mmol) in octadecene (15 ml) in a two neck-RBF. The mixture was heated to 120 °C and kept at this temperature for 60 min without reflux condenser in order to dissolve the reactants and remove the water residues. The condenser was then connected to the flask and the solution was heated to 200 °C (5 °C/min) and kept at this temperature for 10 min. The temperature was then increased to 300 °C (1 °C/min) and heated to reflux for 120 min under air. After cooling to RT, a black gel was obtained. The NPs were washed as previously described.

Synthesis of octopods. Iron oxide nanooctopods (NO) were synthesized from commercial iron stearate (III). $FeSt_3$ (0.735 g, 0.9 mmol) was mixed with OA (1.02 g, 3.6 mmol) in DBE (20 mL) in a two neck-RBF. The mixture heated at 120 °C under stirring and kept at this temperature for 60 min without reflux condenser in order to dissolve the reactants and remove the water residues. The condenser was then connected to the flask and the solution heated to 250 °C (5 °C/min) and kept at this temperature for 60 min. The solution was then brought to 320 °C (10 °C/min) and kept at reflux temperature for 60 min under air. After cooling to RT, a black solution was obtained. The NPs were washed as previously described.

Dendronization of nanoparticles by a direct grafting process. We have already reported the synthesis of the dendron molecule[41–43]. The scheme of the dendron D2-2P is presented in the Figure 1. The dendronization consists in a direct grafting process[43], typically a suspension of 1mL of NP@OA in THF (5 mg/mL) was put in contact with 7 mg of dendron molecule in 4 mL of THF. The mixture was magnetically stirred during 24 h. The NP@dendron were then precipitated by addition of hexane and centrifugation (8000 rpm/min, 3 min). The supernatant was discarded and the NPs were easily dispersed in 10 mL DI water.

The standard protocol was adapted depending on the shape. For all NPs shape, the concentration of NPs was decreased by increasing the volume of the NPs solution at 20 ml instead of 1 ml. Then the time was adapted. 20 nm spheres were put in contact for 48 h. The three other shapes were grafted with a two-step process. After 48 h for the plates and the octopods and 96 h for the cubes[42], the solutions were purified by ultrafiltration to remove the free oleic acid. After 3 steps of purification, the NPs were put in contact with 7 mg of dendron for the same time than the first step.

The NPs@dendrons were then precipitated by addition of hexane followed by centrifugation (8000 rpm/min, 3 min). The supernatant was discarded, and the NPs were easily dispersed in 10mL DI water. The grafted NPs were then separated from the ungrafted dendron molecules by ultrafiltration. After at least 4 purification steps, the pH of the NPs suspensions was adjusted to 7 and the suspensions were ready for characterizations.

The ligand exchange/dendronization was confirmed by infrared spectroscopy and HR-MAS measurements (Figure S1A-C) which showed a very limited amount of remaining oleic acid. The amount of remaining oleic acid was shown previously very important to avoid unspecific uptake of dendronized NPs by cells or in vivo[44].

Glucose coupling. In 5 mL of a NPs solution at 1 mg Fe/mL, 0.3 mmol (80 mg) of glucose (4-aminophenyl β-D-glucopyranoside) and 78 μmol (15 mg) of EDC ((1-Ethyl-3-[3-dimethylaminopropyl]carbodiimide hydrochloride)). After stirring overnight, the NPs were purified by ultrafiltration. After 4 purifications steps, the NPs were ready for characterizations .IR spectrum in Figure S1D confirmed the presence of glucose on dendronized octopods.

Structural characterization techniques

The NPs were characterized by transmission electron microscopy (TEM) with a JEOL 2100 microscope operating at 200 kV (point resolution 0.18 nm). The size distribution of NPs was calculated from the size measurements of more than 300 nanoparticles using ImageJ software. Electron Energy Loss Spectroscopy (EELS) measurements were carried out on a FEI Titan 80-300 Scanning Transmission Electron Microscope operated at 200kV and fitted with an electron monochromator and Gatan Quantum Energy Filter. Data processing of the EELS fine structures to extract the valence state of Fe was carried out using independent component analysis within the Hyperspy open software.

The X-ray diffraction (XRD) pattern was collected at room temperature with a Bruker D8 Advance diffractometer equipped with a monochromatic copper radiation source (Kα = 0.154056 nm) and a Lynx-Eye detector in the 25-65°(2θ) range with a scan step of 0.03°. High purity silicon powder (a = 0.543082 nm) was systematically used as an internal standard. Profile matching refinements were performed through the Fullprof program[45] using Le Bail's method[46] with the modified Thompson-Cox-Hasting (TCH) pseudo-Voigt profile function.

Standard Infrared spectra were recorded between 4000 and 400 cm-1 with a Fourier transform infrared (FTIR) spectrometer, Spectrum 100 from Perkin Elmer. Samples were gently ground and diluted in non-absorbent KBr matrixes.

57Fe Mössbauer spectra were performed at 300 K and 77 K using a conventional constant acceleration transmission spectrometer with a 57Co(Rh) source and a bath cryostat where the sample chamber is under He atmosphere. Further spectra have been obtained using a homemade cryofurnace where sample is maintained under vacuum, whatever the temperature ranged from 77K up to 400°C. The spectra were fitted by means of the MOSFIT program[47] involving

asymmetrical and lines with lorentzian profiles and a □□Fe foil was used as the calibration sample. The values of isomer shift are quoted relative to that of α-Fe at 300 K.

Granulometry measurements were performed on a MALVERN (nano ZS) apparatus for each NP suspension.

The efficiency of ligand exchange was assessed by performing high resolution magic–angle spinning NMR (HR–MAS NMR). HRMAS experiments were carried out on a Bruker FT–NMR Avance 500 equipped with an 11.75T superconducting ultrashield magnet. All the experiments were performed at spinning rate of 5kHz with a 50μL zirconium rotor.

Magnetic Measurements- Experimental setting

DC magnetic measurements were carried out on all synthesized magnetic NPs using a Magnetic Property Measurement System Model 3 (MPMS3) from Quantum Design (QD). Before measurements, the MPMS3 was calibrated using the Pd standard reference sample provided from QD. The calibration was carried out at 298 K following the standard QD procedure for the vibrating measurement mode VSM moment calibration. The VSM calibration factor was adjusted in a way that the difference between calibration measurement and the theoretical value was less than 0.1 %. The MPMS3 measurements were carried out using the QD powder caps and a brass holder. Prior measurements, a blank measurement of the empty brass holder was carried out, but it revealed negligible contribution to the magnetic moment of the sample.

Mass determination: Dry residues of NP suspensions were measured instead of liquid state samples. The iron mass per sample was determined by weighing the NP suspensions before drying and considering the previously known iron concentration. The NP suspensions dried in air at 300 K for about 24 h. The masses were determined with a precision balance from Ohaus (precision 0.01 mg at 0.1 mg, repetition 0.02mg at 0.1 mg) with internal calibration and compensation for air flow and vibrations). The balance is mounted onto an anti-vibration table.

The empty capsule mass was determined 8 to 11 times, the NP suspension mass was determined at least 11 times. On average, the mass of the NP suspension was about 26.29 ± 0.18 mg. Next, the NP volume was calculated using the water density at 25°C. The previously determined Fe concentrations of the suspensions permitted then to calculate the mass of Fe in the dry residue. A direct mass determination of the dry residue was not possible. The measured magnetic moments were then normalized by the mass of Fe in the dry residue.

Magnetization cycles. Four quadrant hysteresis loops were acquired in vibrating measurement mode (VSM) between ± 3 T, using a vibration peak amplitude of 6 mm and an averaging time of 2 s. The field was stabilized at each step before measurement; the field driving rate between steps was set to 10 mT/s. Loops were acquired at various temperatures between 1.8 and 300 K. For some low temperature loops the sample was cooled in a field of +3 T. Each loop consists of about 190 points per branch, which are logarithmically distributed over the ± 3 T range.

AC magnetic measurements: A magnetic characterization of the synthesized magnetic materials was performed under an alternating magnetic field (AMF) in colloidal dispersions (at iron concentration 1.5 g/L) at different frequencies (50, 100, and 200 kHz) and constant magnetic field amplitude (24 kA/m). AC hysteresis loops were traced at room temperature with a home-made inductive magnetometer built by the Advanced Instrumentation Unit (iMdea Nanociencia, Madrid, Spain) which was based on the one described by Connor et al.[48]. The magnetic field was generated by a Litz wire solenoid, inside which two counterwise-wound coils with the same diameter and number of turns collected the induction signal of the sample. The AC magnetization signal was calibrated by comparing magnetization values at similar field intensities which were obtained under AC and quasi-static magnetic field conditions. The AC magnetization signals were normalized to the magnetite mass employed at each experiment.

ZFC/FC experiments. Next, zero-field cooled (ZFC) and field cooled (FC) experiments were performed. Due to the always present residual field of the superconducting magnet, two procedures were tested prior the experiments to limit this effect. A) The field was set to zero in oscillating mode after centring the sample in a 1 T field and B) repeating step A) and subsequent application of a small field opposite to the residual field of the magnet. No difference was observed and therefore procedure A was applied prior ZFC experiments.

The measurements were carried out under the same conditions as the hysteresis loops, i.e. VSM mode, 6 mm peak amplitude and 2 s averaging time. A rate of 5 K/min was chosen for all cooling and warming curves. The magnetic moment was measured continuously during warming and cooling (scanning mode). Data acquisition started after ZFC and 20 min waiting time at 3 K. ZFC/FC measurements were generally acquired in 3 different fields: 5, 10 and 20 mT. Only the curves of sample NC were acquired in different 18 fields from 0.2 to 500 mT.

Magnetic Measurements – data processing

Hysteresis. The measured data was corrected for the residual field of the superconducting magnet. In short, a correction function C(H) was calculated from hysteresis measurements of the Pd standard reference sample. C(H) was then subtracted from the hysteresis measurements of the samples. Also, the high-field slope, caused by dia- or paramagnetic contributions, was determined following the approach to saturation method[49]. This consists in fitting the high-field data between 1 and 3 T resp. -1 and -3 T with the function $a - b\,Hp + c\,H$, with $p = 1$ in the present case. The procedure was applied to all four hysteresis quadrants. Only quadrants with $R^2 > 0.9$ (regarding the fit of the data) were taken to calculate the average high-field susceptibility. Finally, a mean high-field correction was subtracted from the hysteresis data. Saturation magnetization σs saturation remanence σrs and coercive fields at $\sigma = 0$, were obtained from the interpolated, corrected hysteresis data by root finding.

ZFC/FC experiments. ZFC and FC curves consist of about 1800 data points and were filtered with a simple moving average filter with a length of 21 points. The filtered ZFC and FC curves were interpolated linearly to obtain an analytical expression. The derivative of the difference $-[FC(T)-ZFC(T)]$ was calculated and then then digitised. This resulted in a dataset consisting of about 2600 points, which was filtered also with a simple moving average filter of length 21. For data interpretation, the $-[FC(T)-ZFC(T)]$ vs. T curve was used for interpretation.

Magnetic heating measurements. The heat dissipation of NPs suspensions was evaluated with a DM1 system (nB Nanoscale Biomagnetics, Spain) operating at a frequency range of f = 395 – 795 kHz and a field amplitude of H = 4-16 kA.m-1. 1 ml samples were first thermalized for 10 min at 20 °C in the apparatus. Field and frequency were then applied for 5 min.The generated temperature profiles were fitted to the Box Lucas model[50] using the built-in software (nB Nanoscale Biomagnetics, Spain).

Biocompatibility evaluation

Cell culture : Human hepatocarcinoma Huh7 cells were propagated in Dulbecco's modified Eagle's medium supplemented with 10% of decomplemented fetal bovine serum (FBS), 0,5% penicillin and 0,5 % non-essential amino acids.

MTT assay: The number of viable cells after dendronized NPs exposure was evaluated by the MTT (3-[4,5-methylthiazol-2-yl]- 2,5-diphenyl-tetrazolium bromide) assay. In brief, Huh7 cells (1.104 cells per well) were seeded in a 96-well plate and kept overnight for attachment. The next day, the medium was replaced with fresh medium with various concentrations of dendronized NPs diluted in complete culture medium and cells were allowed to grow for 24 h. After completion of incubation, the medium was discarded and well thoroughly washed with 200 μL of PBS in order to eliminate all remaining extracellular nanoparticles. 200 μL of cell culture medium + MTT (0.5 mg.mL-1) is added to each well and cells are incubated for further 3h30 at 37 °C and 5% CO2. After completing the incubation, Medium is carefully discarded and 100 μL of DMSO was

added to each well and incubated 15 min at room temperature under orbital shaking. Color developed after the reaction was measured at 550 nm using Xenius microplate reader (SAFAS, Monaco). Cell viability was obtained as the ratio of mean absorbance of triplicate readings of sample wells (Asample) compared to the mean absorbance of control wells (sample Acontrol). DMSO was used as negative control, ADMSO. as shown in the following equation.

$$Cell\ viability = \frac{A_{sample} - A_{DMSO}}{A_{control} - A_{DMSO}} \times 100\%$$

MRI experiments

Relaxivity measurements T_1 and T_2 relaxation time measurements of dendronized IONPs were performed on a Bruker Minispec 60 (Ettlingen, Germany) working at a Larmor frequency of 60 MHz (1.41 T) at 37 °C. The longitudinal (r_1) and transverse (r_2) relaxivity values were obtained according to the general equation of relaxivity R = R0 + r*[CA], where [CA] is the concentration of the contrast agent (CA) (i.e.) the concentration of Fe in IONPs, R is the relaxation rate (1/T) in the presence of the CA, R0 is the relaxation rate of the aqueous medium in the absence of the CA and r is the relaxivity value of the CA.

Nuclear Magnetic Resonance Dispersion (NMRD) profiles. Proton NMRD profiles were recorded using a Stelar Fast Field Cycling relaxometer (Mede, Italy). The system operates over a range of magnetic field extending from 0.25 mT to 0.94 T (0.01-40 MHz) at 37 °C. T_1 and T_2 measurements were performed on a Bruker Minispec mq60 (Karlsruhe, Germany) working at a Larmor frequency of 60 MHz (1.41T) at 37 °C.

Biodistribution

The MR biodistribution experiments were performed in the MMTV-PyMT (mouse mammary tumor virus-polyoma middle tumor-antigen) mouse model of breast cancer. All animals had free access to food and water and were exposed to standardized conditions. Previous to the measurements the animals were allowed to acclimatize to the ambient conditions for at least 1 week. A total of 4 female mice were used.

Anesthesia was initiated in an animal induction chamber using a mixture of 4% isoflurane (Forene, AbbVie, Wiesbaden, Germany) and 98% oxygen. It was maintained with an animal nose mask applied with a mixture of 1.5% isoflurane (Forene) and 98.5% oxygen at a flow rate of 0.6 l/min. During the measurement the body temperature of the animals was kept stable at 37 °C with a heated water circulating system. Electrocardiogram (ECG) and respiration (spontaneous breathing) were continuously monitored to control the general state of the animals.

The MR scans were conducted using a preclinical 9.4 Tesla scanner (BioSpec 94/21, Bruker, Ettlingen, Germany) and a dedicated mouse quadrature coil with an inner diameter of 38 mm (Bruker, Ettlingen, Germany).

The applied MR scanning protocol consisted of a localizer and a T_2-weighted spin echo RARE (Rapid Acquisition with Relaxation Enhancement) sequence. This sequence was used for anatomical reference and to detect susceptibility artefacts causing signal voids induced by the NPs. The RARE sequence featured a FOV of 30x35 mm²; a matrix size of 256x300 mm². The slice thickness was 1 mm with no slice spacing to achieve contiguous image sets of the whole volume (TR/TEeff/FA: 2000 ms/17 ms/180°, echo train length: 4). For the evaluation of the NPs uptake in the liver, tumor and brain a multi spin-multi echo (MSME) T_2-map was performed to quantify T_2 effects using the same geometry as the T2-RARE sequence, echo time and echo spacing of 8 ms and altogether 10 echo images.

After an initial baseline measurement, a solution of NPs diluted in sodium chloride (0.9%) was injected intravenously into the tail vein of the animals using a self-made catheter (PE-10 tubing, 100cm length). 2 mice were injected octopods NO26 coated with dendron molecules and 2 mice were injected glucose-coupled octopods. The injected volume was adapted for each mouse to standardize the iron

load to 2.5 mg Fe/kg body weight. The catheter was flushed by injecting 100 µl of sodium chloride (0.9%). Subsequently, post-injection scans were performed at time point 30 min, 2 h, 24 h, and 48 h.
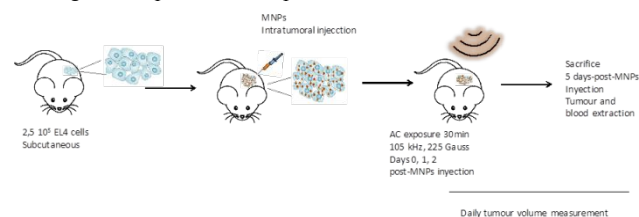
In Vitro and in vivo magnetic hyperthermia

In vitro Huh-7 cells were seeded on a 10 mm cover glass and transferred into a 48-well plate at a concentration of 1.105 cell/well. Cells were incubated for 24 h with Dulbecco's modified Eagle's medium supplemented with 10% of decomplemented fetal bovine serum (FBS), 0,5% penicillin and 0,5 % non-essential amino acids (37 °C in 5% CO2) and then supplemented with a NP suspension (4 mM Fe, 2 ml, complete media) for 24 h at 37 °C in 5% CO2. Cells were then thoroughly rinsed with 2 mL of cold PBS. The cell monolayer was then transferred into a bespoke sample holder and supplemented with complete medium containing 25 mM HEPES. The sample chamber positioned the cell monolayer at the point of maximum field amplitude of the DM1 system (nB Nanoscale Biomagnetics, Spain), while maintaining cell viability. Cells were then exposed for 1h to an AC magnetic field at a magnetic field amplitude of 11.9 – 27.9 kA.m-1 at a frequency of 252 – 796 kHz. Cells were then returned to culture and imaged at different time points with the aid of an Apoptotic/necrotic/healthy cell detection kit (PromoKine). Fluorescence images were captured using Nikon Elipse TE200 with 63× PL APO (1.4 NA) objective equipped with Nikon Digital Camera (DS-Q11MC with NIS-Elements softwares), and processed with ImageJ (http://rsb.info.nih.gov/ij/).

In vivo Magnetic hyperthermia. Female 6-week C57BL/6 mice were commercially obtained (Charles River) and after a week of acclimation 2,5 105 EL6 cells in 100 µL cell culture medium were injected subcutaneous in the right flank with a 25G needle. After 7 days tumors were small but big enough to inject NPs intratumorally. 70 uL of a sterile (passed through a 0,2 µm filter) 2,6 ± 0,2 mgFe/mL (in PBS) MNPs solution were injected intratumorally per mice (about 182 µgFe/tumor) with a 30G needle. NPs injection was performed in one point of the tumor. The same day of NPs injection and the following two days mice were exposed to alternating magnetic fields (AMF) using a commercial device from NanoScale Biomagetics company (DM3 model). Each AMF application consisted of 30 min exposure time at 105 kHz and 18kA/m2. Mice were anesthetized with isofluorano and were maintained during the AMF exposure onto a hot water bath system that prevent the mice to suffer hypothermia. Rectal temperature was registered during the AMF exposure to control general state of the animals.

Tumor dimensions (length, with and height) were daily measured with a caliper and also mice weight was recorded. Tumor growth was calculated as (Tumor Volume)/(Initial Tumor Volume). After the last AMF exposure mice were maintained 3 days or until tumors started to ulcerate.

Mice were euthanasiated by CO2 inhalation and blood was directly extracted from the heart and tumor was removed and fixed in 4% PFA and processed to perform Hematoxylin/Eosin staining and Blue Perls staining. The experiment is depicted in Scheme 1.

Scheme 1. Experimental set up for in vivo magnetic hyperthermia

MH Experiments with NPs coupled with glucose. Similar *in vivo* MH experiments were made with NPs coupled with glucose. Trying to observe the antitumoral effect at longer port-treatment times in human derived calcer cells lines some experimental details were modified. Male 6-week nude mice were commercially obtained and after a week of acclimation 2 10⁶ HCT-116 (human colorectal cancer

cell line) cells in 100 μL DMEM were injected subcutaneous in the left flank with a 25G needle. After 12 days 100 μL of a sterile 2 mgFe/mL (in PBS) NPs solution were injected intratumorally per mice (200 μgFe/tumor) with a 30G needle. Besides, AMF conditions were also tuned for using higher frequency and amplitude but maintaining the $H_0 x f$ value below the biological safety limit (196 kHz and 26 kA/m).

3. Results and discussion

3.1 Structural characterization of iron oxide NPs of different sizes and shapes

Iron oxide NPs with various morphologies were synthesized through the thermal decomposition process[25,51]: spherical NPs (NS) and three anisotropic shapes: nanocubes (NC), nanoplates (NPl) and nano-octopods (NO) named NS18, NC16, NPl20 and NO18 respectively. Nanospheres were synthesized in order to highlight the effect of shape anisotropy and because this diameter has been reported optimal for magnetic hyperthermia[9]. Transmission electron microscopy (TEM) images of the spheres (NS18 and NS22), cubes (NC16), octopods (NO18) and plates (NPl20) are illustrated in Figure 1. Nanospheres and octopods of different size have also been synthesized for investigating potential size effects. The structural characterizations performed on NS22, NC16, NO26 and NPl20 samples by XRD and IR spectroscopy (Figure S2 and Table 1) showed that all the synthesized NPs present a spinel structure close to the magnetite Fe_3-xO_4 composition except NC16 that displays a core-shell $Fe_1-xO@Fe_3-xO_4$ composition, as previously described [25,51,52]. The lattice parameter and crystallite sizes have been determined from Rietveld refinement of XRD pattern and are given in Table 1.

Nanocubes are core-shell structures with a core of the antiferromagnetic (AFM) Fe_1-xO shelled by a ferrimagnetic (FM) Fe_3-xO_4. The experimental conditions have been tuned in order to obtain nanocubes with a homogeneous spinel composition but without success. Our recent investigations demonstrated that our synthesis conditions, necessary to provide the cubic shape, are always strongly reducing and when a spinel composition has been obtained by introducing benzyl ether as in works of Pellegrino et al.[19], the shape was not cubic with straight faces but octopod[25,51]. This demonstrates again that the mastering of NPs shape and composition is always a challenge. It was expected that the exchange bias between the AFM core and FM shell would add a supplementary anisotropy suitable for MH. However it has also been often reported that the Fe_1-xO phase deteriorates the overall magnetization of the particles, thus jeopardizing their hyperthermia efficacy[53].

NS22 NPs have a composition close to the magnetite one. However, its crystallite size is lower than the mean size determined in TEM images. This is related to the presence of defects inside the NS volume. Indeed, it is now well known that nuclei formed during the thermal decomposition process have a wüstite Fe_1-xO composition and thus the magnetite composition of NS results from oxidation of the wüstite phase during the synthesis process. However the oxidation of Fe_1-xO has often been reported to generate defects such as dislocation or antiphase boundaries[25,54,55] and it was again demonstrated recently by Pellegrino et al.[53]. In Figure 2, some defects have been evidenced by performing a FFT treatment of HRTEM image. Such defects may also be responsible for the observed lattice parameter very close to the magnetite ones[52]. Indeed the investigation of the oxidation of $Fe_1-xO@Fe_3-xO_4$ nanocubes detailed in ref[52] has shown that stresses are generated at the core-shell interface and within the spinel shell due to the epitaxial growth and oxidation mechanisms of the wüstite phase. A higher lattice parameter than that of the stoichiometric magnetite was noticed and attributed to the presence of these defects induced by the oxidation. To be sure that the composition of NS was really the magnetite one, IR spectroscopy and Mössbauer spectroscopies are the most adapted techniques to discriminate between magnetite and maghemite phases. Mössbauer spectroscopy will be detailed below but the Fe-O bands in IR spectra (Figure S2e-f) displaying a main band at 580 cm-1 with a shoulder towards larger wavelengths are characteristic of a slightly oxidized magnetite phase confirming again that the composition of iron oxide phase cannot be ascertained only from XRD pattern.

For octopods (NO) and nanoplates (NPl), the crystallite size is strongly dependent on the crystallographic directions. For NPl, a crystallite size of 20 nm was found along the <222> direction confirming that this morphology is composed of a single crystallographic domain. Along the <400> direction the crystallite size is found to be 5 nm close to the thickness of the plate. However SAED patterns show slightly extended spots which support the presence of defects and/or strains[56].

For octopods NO, the composition is closer to that of maghemite from consideration of the lattice parameter and a crystallite size of 25 nm is calculated along <400> and of 23 nm along <511> for NO26. The fact that the crystallite size relies on a specific crystallographic direction is in favor of a stronger anisotropy for those shapes with different shape factor. Investigations of defects by HRTEM and inverse FFT showed the presence of few defects in octopods in agreement with their more oxidizing synthesis conditions (presence of polar solvents) by comparison with other shapes.
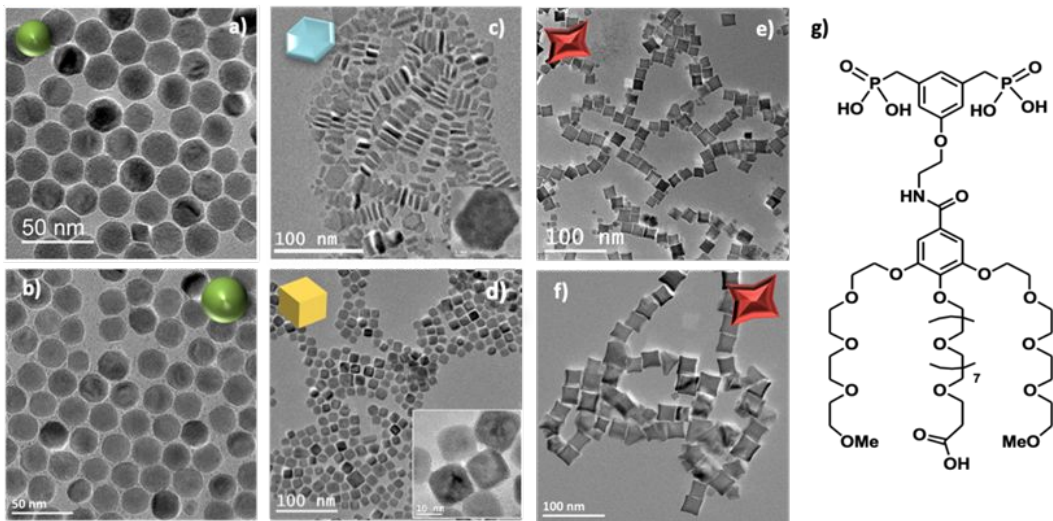
Figure 1. TEM images of iron oxide NPs with different shapes and sizes: NS18 a), NS22 b), NPl20 c), NC16 d), NO18 e) and NO26 f) and Scheme of the D2-2P dendron molecule g)

Table 1. Main structural parameters of the different shaped NPs from IR and XRD measurements

NPs	Mean TEM size (nm)	Crystallites size (nm)	Lattice parameter (Å)		Composition
			Spinel phase	Wüstite phase	
NS22	22 ± 2	13	8.391	X	$Fe_{3-x}O_4$
NC16	16 ± 2	8	8.392	4.237	$Fe_{1-x}O@Fe_{3-x}O_4$
NO18	17 ± 2	15 <220> / 15 <440>	8.364	X	$Fe_{3-x}O_4$
NO26	28 ± 4	25 <400> /23 <511>	8.370	X	$Fe_{3-x}O_4$
NPl17	20 ± 7 nm // 6 ± 2	20 <222> / 5 <400>	8.384	X	$Fe_{3-x}O_4$
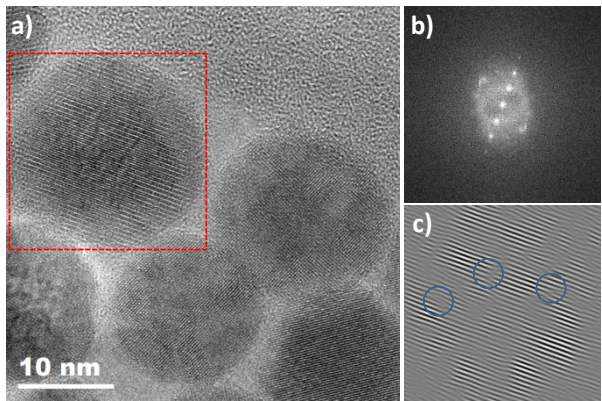
Figure 2. Defects in NS22 NPs (zone axis [110]): a) HRTEM NS22 image and b) fast Fourier transform (FFT) image obtained from the analysis depicted by the red square. c) Inverse of the FFT obtained by selecting the {220} family plan showing the presence of defects.

3.2 Structural and magnetic characterisations of dendronized nanoparticles

3.2.1 Structural characterisations.

As described in Section 2, NPs have been then coated with dendron molecules by a direct ligand exchange process consisting in introducing dendron molecules in a THF suspension of NPs coated with oleic acid[41–43]. By contrast with 10 nm sized nanospheres, the dendronization process had to be optimized for each shape due to variation of the surface to graft. The effect of this dendronization step on iron oxide NPs composition and properties has been then investigated.

^{57}Fe Mössbauer spectrometry has been used to discriminate the different Fe species and to determine their respective oxidation states from the isomer shift values. Mössbauer spectra have been retrieved from all dendronized NPs (except nanocubes consisting in core-shell $Fe_{1-x}O@Fe_{3-x}O_4$), but some experiments have been also performed on oleic acid coated NPs for comparison. It is important to emphasize that the following Mössbauer spectra were recorded on samples containing very small quantities (2-5 mg) of powders after focusing with a lead mask to get an efficient surface containing about 5 mg Fe/cm2.

The Mössbauer spectra of all dendronized NPs at 300 K and 77 K look a priori quite similar as all of them exhibit magnetic sextets in addition to a small quadrupolar feature at the center (see Figures 3 and S3). At 300 K, the lines exhibit some asymmetrical broadening resulting from intrinsic electronic properties but due to the NPs size, superparamagnetic doublet should be observed at 300K. Magnetic measurements presented below confirmed a superparamagnetic behavior of our NPs. In fact, we are in the particular case where NPs with relaxation times between 140 ns (measurement time of Mössbauer spectrometry) and 1 s (measure time for a single point of a hysteresis curve) would be seen as non-superparamagnetic in Mössbauer, but as superparamagnetic in hysteresis loops. From relaxivity measurements in Table 4, the relaxation times deduced from this range roughly between 0.002 and 0.2 s, which is much larger than the characteristic observation time of Mössbauer and below the observation time of the hysteresis measurements.

Thus, the magnetic component has been described by means of several magnetic sextets with different isomer shift values. They are ranged from 0.3 up to 0.45 mm/s, attributed to Fe

ions with different oxidation states between Fe3+ and about Fe2.7+. That confirms a composition corresponding to an oxidized magnetite. One first way is to estimate the mean stoichiometry of each set of NPs. Those results can be also modelled in terms of a core-shell model which consists in stoichiometric magnetite and maghemite phases, as previously described in [16,57]: the proportions allow the thickness of the maghemite shell to be estimated, dependently on the mean morphology of NPs. Table 2 summarizes the mean values of hyperfine parameters corresponding to the present types of NPs after dendronization. In addition, the central part is better described by adding a quadrupolar component assigned to HS Fe3+ species. At this stage, this small component could be attributed to the presence of Fe species connected to dendrons, originating some local Fe environments close to those of iron phosphate compounds. At 77K, the spectra are composed of lines which are narrower than those observed at 300K. Different fitting procedures were considered to describe those spectra: in the case of nanoplates, it consists in using only two magnetic components, in addition to a quadrupolar component. The values of isomer shift are rather consistent with HS Fe3+ species. Thus, the nanoplatelets consist essentially in maghemite resulting from the significant oxidation of magnetite, favored by their large surface/volume fraction. The spectrum characteristic of octopods exhibits some broadening of the internal wings of the outer lines which have to be described by means of several magnetic sextets with different isomer shift values: consequently, the octopods consist of a non-homogeneous phase, the stoichiometry of which should vary continuously from magnetite at the center and maghemite at the surface. In the case of the nanospheres, one observes some shoulder in the internal wing of the 2nd and 6th magnetic lines, in contrast to the other two samples. This feature can be likely assigned to a blocked HS Fe2+ species which would confirm that the nuclei of NPs consist in wüstite which oxidizes leading to magnetite-maghemite core-shell structure with defects. Mössbauer spectra have also been recorded under an applied field of 8T at 12K on the three samples and are compared in Figure 3b. Using such instrumental conditions, the magnetic sextets are well split into two main magnetic sextets which can be unambiguously attributed to tetrahedral and octahedral Fe sites, according to the ferrimagnetic structure. Their resolution leads to accurately estimate the proportions of tetrahedrally and octahedrally-coordinated Fe3+ species: for the three samples, the ratio tetra:octa is found rather close to 1:2. In addition, the corresponding isomer shift values are also suitably consistent with those observed at 77K and 300K. However, a better refinement is obtained by means of a third magnetic component to describe the internal wings of magnetic lines: the larger value of isomer shift suggests the presence of Fe species with valency states intermediate between 2 and 3, in perfect agreement with zero-field results as above mentioned.

The last information is concerned by the intensity of intermediate lines which is related to the canting of magnetic moments respect to the external magnetic field. The canting appears usually lower for Fe3+ species located in tetrahedral sites (<10°) than those in octahedral sites (10-20°) while that of the third component exceeds 30°. This later value is consistent with a non colinear magnetic structure in the bulk originated from the magnetic frustration resulting from the combined effects of the cationic topology correlated to the local stoichiometry and the magnetic anisotropy of Fe2+. In the case of nanospheres, the thickness of the canted layer is estimated at about 0.5 nm for the octahedral sites and close to zero for tetrahedral ones, suggesting that the surface results preferentially from octahedral units. The global magnetic structure remains rather similar in the case of octopods, with a larger canting which can be due to the morphology. On the opposite, the magnetic structure of nanoplatelets appears less canted, only the non-stoichiometric internal layer because of its structural and topological nature.

The particular cases of nanospheres, nanoplates and octopods were further probed by TEM-EELS analyses. With the NS22 NPs, the EELS analysis performed on several NPs showed that the Fe valence is almost the same in the core of NPs and at their surface. Two typical spectra obtained by separating the EELS signals corresponding preferentially to the two core and surface regions are shown in Figure S4. While the energy position of the peak did not change, they appeared to be a slight broadening of the Fe L23 edge. This effect could be due to the presence of Fe linked to the ligand molecules.

The EELS analysis performed on NO26 (Figure 4) showed that the core of NO contained a larger relative amount of Fe3+ atoms comparing to that of Fe2+, while the surface has more a Fe2+ component (Figure 4). That allowed us to conclude that for all the analyzed NPs the surface layer would have a lower valence than the core one. The inhomogeneous distribution of the Fe2+ and Fe3+ components through the particle could be the result of either the presence of a very localized Fe1-XO phase or a mixed oxide with reduced valence. It should be mentioned here that, as the spectra acquired at this edge are relatively noisy, it is difficult to properly determine an eventual change in the spectral shape through the particle. This analysis would confirm Mössbauer results that the composition of octopods is inhomogeneous and evidences a surface effect.

The same type of analysis of the EELS spectra acquired on nanoplates (Figure S5) provided similar results: the surface of NPls also showed a reduced valence of Fe on the surface as compared to the Fe valence in the core.

However, the difference in the corresponding EELS spectra characterizing the core and surface difference is less important than in the case of the octopods. In addition, the Fe spectrum extracted from independent component analysis on the core did not exhibit the same shoulder as in the case of the octopods.
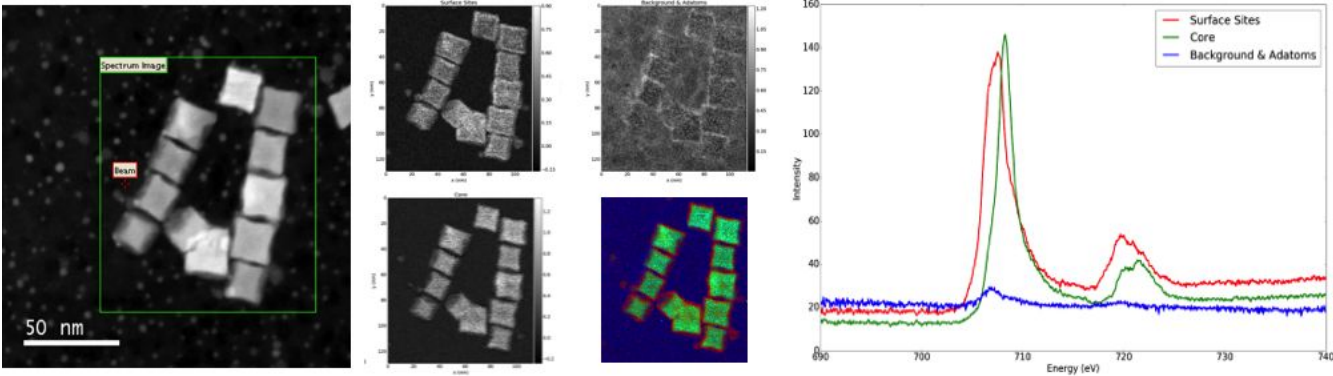
Both TEM-EELS analysis and Mössbauer spectroscopy support that the composition of octopods is rather different (inhomogeneous) from that of isotropic NPs and that the surface of octopods and nanoplates is rather different from that of isotropic NPs.
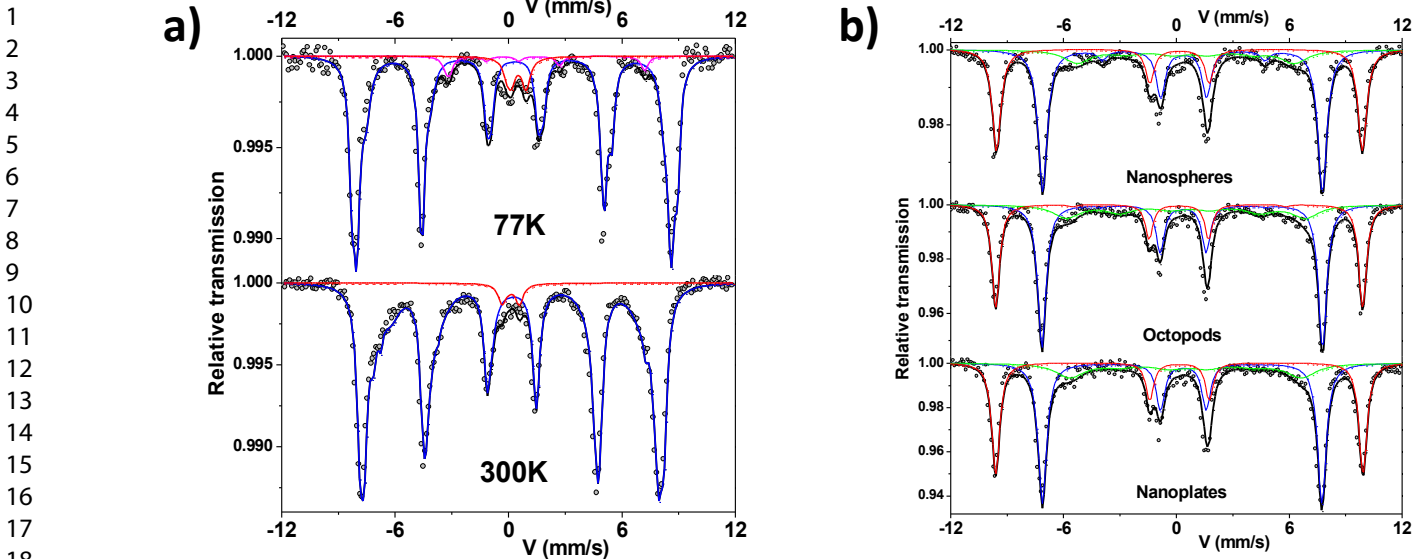
Figure 3. a) Representative 300 K and 77 K Mössbauer spectra of sample NS22 (blue: sextet, red: doublet, pink: quadrupolar component) and b) Mössbauer spectra of samples NS22, NO18 and NPl20 under an applied field of 8T at 12K.

Table 2. Mean values of hyperfine parameters refined from Mössbauer spectra recorded on NPs with different shapes (IS : isomer shift, BHF: hyperfine field, stoichiometry "3-x" in Fe3-xO4, <e> thickness of the maghemite shell, <t> thickness of the canted layer for tetrahedral and octahedral sites)

	<IS> mm/s ± 0.01	<B_{hf}> T ± 0.5	γ–Fe_2O_3 (%) ±3	Fe_3O_4 (%) ±3	<Stoichiometry> ± 0.02	<e> $_{\gamma-Fe2O3}$ nm ± 0.5	<t> nm ± 0.5
NS22	0.524	50.5	60	40	2.80	3.7	0 – 0.5
NO18	0.483	51.4	79	21	2.74	2.5	0.1-0.1
NPl20	0.451	52.0	94	6	2.68	4.0	0-0

Figure 4. EELS analysis of several NO26 NPs: HAADF image of the chosen NPs, along with the decomposition of the Fe L23 edge EELS signals in their different contributions as extracted via independent component analysis. The individual maps show the spatial distribution of the surface, core and background signals (central panel) with the corresponding spectra of the surface layer (red spectrum), core (green spectrum) and the background and ad-atoms (blue spectrum). In the central panel shows the respective spatial maps of the separated components with the colour coded map showing the superposed overlapping images of these separate contributions (surface components (red), core components (green)and background with adatoms on the support film (blue)).

3.2.2 Magnetic characterizations

The ZFC/FC curves (Figure S6) of all NPs are characteristic of superparamagnetic-like NPs with an average blocking temperature located at the surroundings of the maximum T_{max} of the ZFC curve. The corresponding temperature derivatives of the ZFC curves (Figure 5 and Figure S6) allowed identifying the most distinct peaks whose values are given in Table 3 featured by each sample. This analysis is important to confirm the structural characterisation previously presented, since all the iron oxide phases involved present unique magnetic features that can be detected through a careful appraisal of ZFC/FC curves. Likewise, the evolution of magnetization with temperature is key to identify other

relevant aspects of the nanoparticle magnetism that directly affects the total anisotropy energy of the different samples.

Except in the specific case of sample NC16, the broad intense peak P1 (Figure 5; Table 3) showed a marked field dependence, which means that it corresponds to the blocking process of most of NPs within the sample but not all of them due to the size distribution always present to a variable extent. P1 shifts towards lower temperatures as the field increases because the probing field decreases the anisotropy barrier the NPs have to overcome during their unblocking process. Consequently, the population of unblocked NPs at the lower end of the temperature range increases for higher applied fields. Therefore, this peak can be assimilated to the average blocking temperature of NPs.
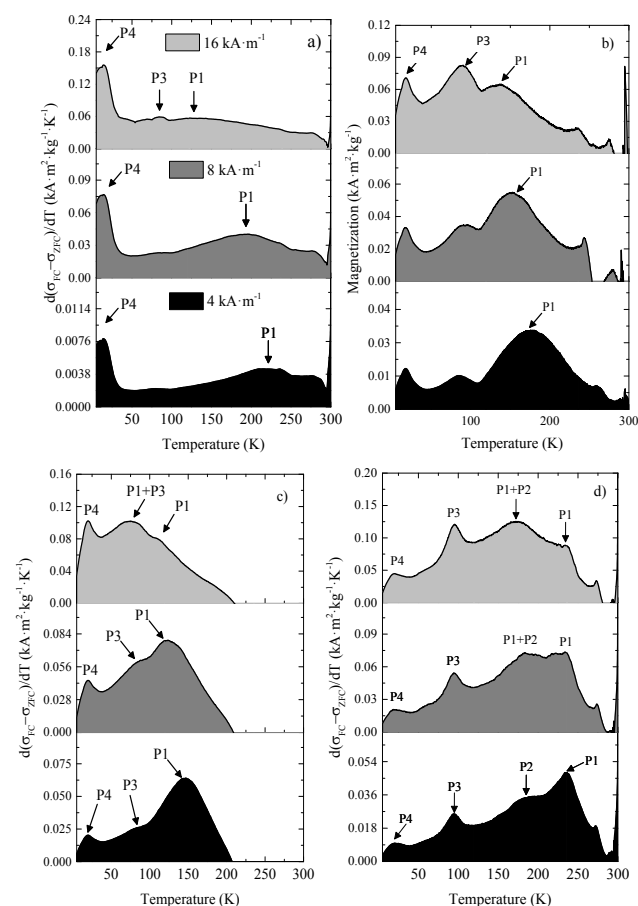
Figure 5. Differential ZFC magnetization curves with respect to the temperature for samples a)NO18, b)NS18, c)NPl20 and d)NC16 , obtained at external fields of 4, 8 and 16 kA·m^{-1}.

Peak P2 is only present in sample NC16. Since these NPs consist of a core of wüstite (Fe$_{1-x}$O) with an oxidized shell (Ɣ-Fe$_2$O$_3$) at the surface, P2 can be attributed to the Néel temperature (T_N) of Fe$_{1-x}$O. The intensity of P2 in Figure 5 progressively increases at the expense of that of P1 for increasing applied fields. A small fraction of NPs still contributes to P1 even at 16 kA·m^{-1}. Incidentally, P2 undergoes an apparent intensity increase in sample NC16 which is only due to its partial overlap with P1 while shifting towards lower temperatures (Figure 5.d).

Table 3. Assignment of the peaks observed in the differential ZFC/FC curves in Figure 5 with indication of the corresponding temperature values in Kelvin.

		Sample				
Peak #	Field (kA·m^{-1})	NS18	NO18	NPl20	NC16	Assignment
P1	4	180	225	150	240	T_{max}
	8	162	193	122	220, 240	
	16	156	128	112	175, 240	
P2	4	--	--	--	175	T_N (FeO)
	8					
	16					
P3	4	90	90*	90**	90	T_V
	8					
	16					
P4	4	20	20	20	20	T_f
	8					
	16					

* Very weak; only at the highest applied field.

** Very weak.

Peak P3 does not show a field dependence, although it becomes more intense for higher applied fields. It corresponds to the Verwey transition of magnetite (T_V), and it is confirmed by the small bump in the FC branch at the same temperature (Figure S6). Although this transition is expected to occur at higher temperatures in the bulk phase, it has been reported that it shifts towards lower temperatures for smaller particle sizes[58], similarly to the experimental observations for the Morin transition in hematite nanoparticles,[59] which even disappears for sufficiently small NPs.[60] Other explanation are also a deviation from stoechiometry of the magnetite phase : T_V has been reported to be very sensitive to the stoichiometry, because the Fe vacancy increase in the Fe$_{3-x}$O4 leads to a decrease in the strength of the Fe-Fe exchange on B sites. Indeed, T_V is reported to decrease from Fe$_{2.995}$O$_4$ at 125 K to Fe$_{2.934}$O$_4$ at 100 K[16]. The progressive intensity increase of P3 is merely incidental, and stems from the shift of P1 at increasing fields (Figure 5.c). As mentioned, the Verwey transition is usually seen as an abrupt jump in both ZFC and FC magnetization, which is observed in NS22 and NO26 (Figure S6 b&e). With samples NO18 and NPl20, we only see a modest peak that is suggested to be due to a lower content of magnetite in the NPs as confirmed by the above structural characterizations (they are oxidized into maghemite to a sizeable extent).

Peak P4 does not depend on the applied field, and given the low temperature at which it appears, it is ascribed to the spin-glass-like behavior of the superficial spins, more precisely to their freezing temperature (T_f). The field is not able to contribute to their blocking process, and only very low temperatures can freeze them and block their magnetic moments. One may notice that this peak is clearly more visible for NO18, NO26 and NPl20 and suggested a higher canting degree on the surface spins compared to other samples. It

would confirm TEM EELS and Mössbauer results on a more complex surface state of octopods.

Magnetization ($\sigma(H)$) curves at room temperature of all NPs are characteristic of a superparamagnetic regime (Figure S7)—i.e., zero coercivity and remanence—, while a ferrimagnetic behavior is realized at 5K as expected for NPs below their blocking temperature. To evaluate the occurrence of exchange interactions between the core of NPs and a canted layer of spins at the surface $Fe_3O_4@Fe_3O_4$ or $Fe_3O_4@Fe_xO_y$[31] field-cooled magnetization curves FC (M(H)) have been further recorded, and an exchange field H_{bias} characteristic of such exchange has been determined (Figure S7). The methodology has been described elsewhere[61].

The general trend of H_{bias} with temperature (Figure S8) is a small and positive exponential decay towards higher temperatures in all samples. Due to its core-shell structure with an antiferromagnetic core and a ferrimagnetic shell, NC16 is the sample exhibiting the most noticeable exchange bias effect throughout the entire sample series (Figure S8). The intensity of the H_{bias} is of course above than that expected for just the contribution of surface spins. Indeed, the H_{bias} is quite high now because the presence of the exchange bias interaction between the antiferromagnetic $Fe_{1-x}O$ core and the ferrimagnetic $Fe_{3-x}O_4$ shell. We had already observed earlier this effect in such core-shell nanocubes[52].

In the inset of the FC hysteresis loop at 5 K of NS22, it can be observed the so-called "wasp-waisted" behaviour (Figure S7, insert). This effect has been traditionally associated with the coexistence of multiple phases although it has been also proposed that it may well be due to the apparition of two switching fields in a single phase sample[62]. Such duality would stem from the combination of interparticle interactions (for example due to a concentration increase) with easy-plane anisotropy, which correspond to a negative first anisotropy constant, as opposed to the uniaxial anisotropy (positive first anisotropy constant) typically considered in systems of single-domain and superparamagnetic NPs. The subtle wasp-waisted hysteresis effect on the sample is also compatible with the existence of a residual multi-domain fraction. These results are in agreement with the structural characterization, since we have shown from XRD measurement that the coherence length was smaller than the TEM size. The exchange bias observed here is due to a surface and volume spin canting[31]. Otherwise the exchange bias values for NPL20 are lower than those of NO18 confirming quite low spin canting in agreement with Mössbauer spectroscopy.

The temperature dependence of H_C (Figure S9) is qualitatively similar to that found by other authors in other nanoparticle systems[63] and subsequent theoretical calculations[64], and it fits to a radial surface anisotropy model quite well. This form of anisotropy adds to the uniaxial anisotropy borne by the inner spins of each NP, and its value is mainly determined by the exchange coupling between both types of spins—inner and superficial ones—and by the angle formed between the applied field and the easy anisotropy axis. H_C shows a rather monotonic increase with decreasing temperatures for values up to ≈100 K. From this point onwards, H_C increases at a much faster rate as the spin freezing temperature of the superficial spins approaches; around 20 K, as revealed by the corresponding ZFC curves in Figure S6 almost doubling its value within the last 50 K. Nevertheless, from T=20 K, H_C does not increase noticeably,

which coincides with the temperature where all the spins—including the superficial ones—are assumed to be fully exchanged and also aligned with the external field. Additionally, since $Hc \propto K/\sigma_s$, and both K and σ_s are intrinsic properties given by the crystalline structure of the material, the observed deviations may in principle be ascribed to structural changes or finite-size effects that may affect both K and σ_s. H_c values reveal that sample NO18 show the lowest coercivity change from 300 K down to 5 K. Given the dependence of H_C on particle volume, this fact indicates that this sample has the lowest population of blocked NPs, or in other words, most of their constituent NPs are already unblocked at room temperature. NO18 present the lowest Hc and then arrive NS22 and NPl20.

To better evaluate the heating mechanism and if it is related either Neel and/or Brownian relaxation, magnetization curves have been recorded at different frequency and also in media with different viscosity (Figures 6 and S10-11)[65,66]. AC hysteresis loops at 100 kHz showed very distinctive AC magnetic patterns depending on sample size and shape. Octopod NPs presents the largest opening of the AC hysteresis loops, whereas NPl20 the lowest. Indeed, the area of curves showed that the heating efficiency of spherical iron oxide NPs improved upon increasing particle size whereas the nanoparticle shape has a remarkable effect on the dissipated heat by the system under AC fields. At the same time, the hysteresis opening reveals further qualitative information related to the magnetic anisotropy. The AC hysteresis loops observed for NO26 are not well developed in comparison to NPs with different sizes and shapes. Indeed, the AC hysteresis loops of NO26 has a wide elliptical shape whose coercitive field is close to the maximum external field intensity. Such AC hysteresis loops are characterized for minor loops due to large magnetic anisotropy values[65].

Large anisotropy values also influence the prevalent magnetic relaxation processes[65] [and reference there in]. Thus, Brownian relaxation typically dominates for large anisotropy or NP size. The prelavance or contribution of Brownian process into the effective magnetic relaxation mechanism can be clearly observed when media viscosity is tuned. (Figures S10-11) Thus, our results suggest that the Brownian motion is the main heating mechanism for NO26, and the Néel-one prevails for the other NPs.
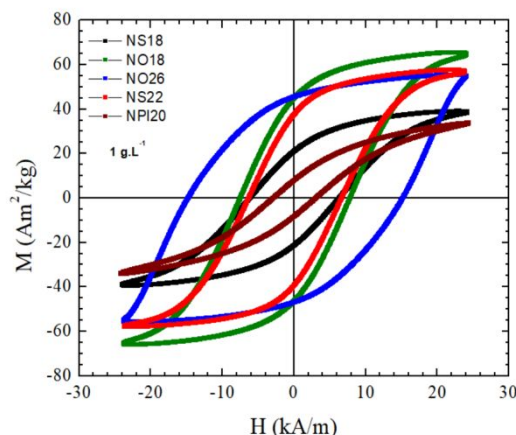
Figure 6. AC hysteresis loops obtained at 100 kHz and 24 kA/m for water dispersions of NS18, NS22,NO18, NO26, and NPl20 at 1 g_{Fe}/l.

3.3 In vitro investigations of dendronized nanoparticles

The colloidal stability of NPs in different physiological media has been assessed with DLS measurements (Figure S12). The mean hydrodynamic diameter is only indicative of potential aggregation for NPs displaying other shapes than the spherical one as the optical model used to calculate the size distribution considers spherical NPs. Anisotropic NC, NO and NPl may be present in front of the laser under different orientations that can be longer than the edge length or the diameter. Therefore, the values of mean hydrodynamic diameter are just given for comparison and cannot be considered as accurate. The mean hydrodynamic size of dendronized NPs is below 60 nm except for NC (Table 4). Indeed, NC16 display after dendronization the highest mean hydrodynamic diameter (Table 4) and a broad hydrodynamic size distribution. Dendronized NC16 tend to flocculate with time as opposite to the other NPs although they can be easily re-dispersed under weak sonication.

Then relaxivity and SAR measurements have been performed on the dendronized NPs suspensions. The main properties are summarized in Table 4 and in Figures S13-14. A good T_2 contrast agent is expected to display both a high r_2 value and a high r_2/r_1 ratio[8]. NC display the lowest r_2 and SAR values, whereas NPl display high r1 and r2/r1 values similar to those of NS18 but low SAR value. NS22 display higher relaxivity values as well as SAR values by comparaison with NS18 as expected with such isotropic NPs which Ms increases with the NPs size[31,67]. By contrast, NO18 show a higher r_2 and SAR values than NO26. All dendronized NPs can be used as contrast agent for MRI. For MH, the best performances are reached by nanospheres and octopods.

As expected and shown in Figure S13 for NO18 and NS18, SAR values increase when frequency and/or magnetic field amplitude increase. No heat dissipation was observed for nanoplates and nanocubes with fields below 12 kA/m and low frequency (below 796 kHz). Heat losses were observed at all tested frequency and magnetic field for octopods whereas no significant heat loss was measured for spherical NPs at 4 kA.m^{-1}.

As the amount of *in vivo* internalized NPs may be low after intravenous injection, the effect of NPs concentration on SAR values has been investigated (Figure S14) and evidenced that even at low concentration, octopods present high heating values. The heating performance of NS18 is also preserved at quite low concentration. As it can be noticed from these data, octopods show the best properties in terms of relaxivity and SAR values even at low concentration (Figure S14) regardless of particle size

.

Table 4. Main MRI and magnetic heating properties of the different shaped NPs in water suspension (D_h is the mean hydrodynamic size). SAR value for NO18 at 1 mg.ml^{-1} may not be accurate as evaporation occurred due to the elevated temperature but as shown in Figure S13, the SAR values remain the highest even at lower AMF.

NPs	Mean length of longest axis (nm)	D_h (nm)	Relaxivities at 1.41T mM.s^{-1}			Specific Absorption Rate (SAR) (± 20 W/g$_{Fe}$) f=796 KHz.and H=16 kA.m^{-1}	
	TEM	DLS	r_1	r_2	r_2/r_1	C= 1 mg/mL Fe	C= 0,5 mg/mL
NS10[54]	10	18	13	78	6	No heating	No heating
Resovist	3-5	62	9.7	189	19.5	-	-
Endorem	ND	120-130	10	141	14	-	-
NS22	22.2 ± 1.8	28	10	303	30	395±20	425±20
NS18	17.9	35	12	189	16	300	350
NC16	15.9 ± 1.8	94	5	138	28	65	90
NO18	17.2	51	17	405	24	950	1000
NO26	26.1 ± 4	60	8	274	34	528	ND
NPl20	20 ± 7 nm // 5.7 ± 1.6	84	15	265	17.7	90	120

The determination of the NMRD profile of a contrast agent consists in measuring the relaxivity r_1 at different magnetic fields. Obtained by a fast field cycling method, it allows a fast analysis of the properties of a contrast agent and determines in which frequency range / magnetic field it will be most effective NMRD profiles have been recorded for all the shapes and are represented in Figure 15. NC16 and NPl20 present the typical profiles expected for superparamagnetic NPs. The relaxivities of NPl are low compared to those of NC16 despite the possible influence of the antiferromagnetic Fe$_{1-x}$O core for NC. The value of the r_1 maxima at high frequency is lower for NPl than for NC16 suggesting a lower saturation magnetization of nanoplates by comparison with nanocubes.

NS22 and NO26 present a different behavior. The bump/maximum observed around 1-3 MHz for NC16 and NPl17 disappeared. The position of this bump is dependent on the size of the NPs. The profile of the NS22 can be thus explained by their size (22 nm) and some chains formation happening under the applied magnetic field in agreement with a spontaneous chain alignement observed when NS are deposited on TEM grids (Figure S15) and during NPs deposition experiments on substrates[68]. Such anisotropy would explain their high relaxivity and SAR values (Table 4). Both NO profiles present high relaxivities at low field. This is not explained by the NMRD theory, which was developed for symmetrical systems[69]. Since anisotropy energy controls the NP behavior at low field, and the observed high relaxivities values may be explained by the fact that NO display a high

anisotropy energy (see the anisotropy calculations made in the supplementary information). Unfortunately, no theoretical model was developed for such kind of structures to date. Furthermore octopods may also align during the measurements increasing thus their anisotropy, but another hypothesis could be that their peculiar shape with elongated corners induces local magnetic field heterogeneities which affect positively relaxivity values. These profiles evidenced thus a high anisotropy in these systems especially for octopods. That would explain the high relaxivity and SAR values observed for octopods by comparison with nanospheres: there is a contribution of the shape anisotropy and anisotropy induced by their alignment under AMF.
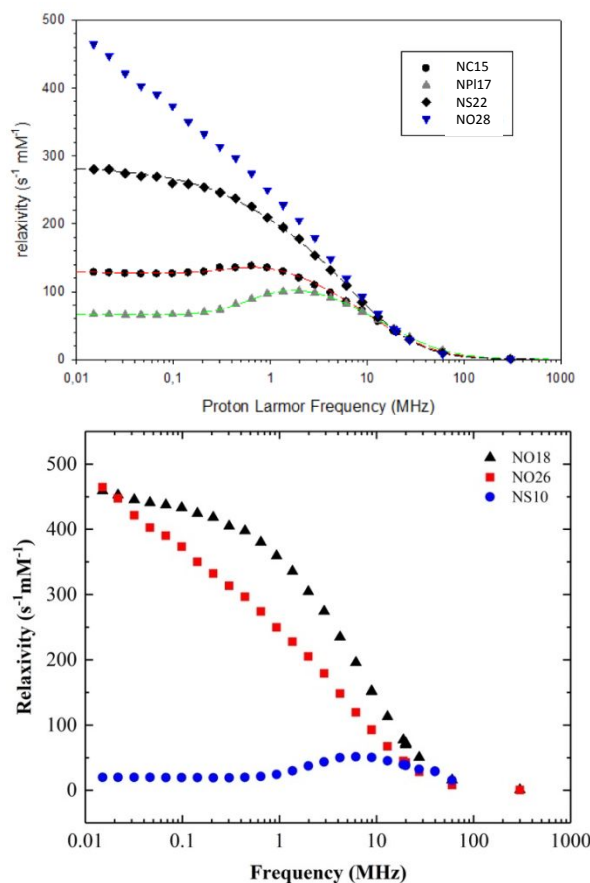

Figure 15. NMRD profiles of the different shaped NPs (NS10 corresponds to iron oxide NPs with a mean diameter of 10 nm and dendronized).

Due to their excellent performance in magnetic hyperthermia and imaging, the octopod-shaped NPs have been selected for further *in vivo* investigations.

3.4. *In vivo* MRI and cellular and *in vivo* magnetic hyperthermia with dendronized octopods

3.4.1 *In vivo* MRI

Biodistribution of octopods NO26 coated with dendron molecules and of glucose-coupled (for enhancing tumor internalisation) dendronized octopods was investigated over 48 hours (Figures 16 and S16). NO26 were selected due to their higher hydrodynamic size and since they were used for MH experiments also. The contrast change in the liver implies a high NP uptake within the first 2 hours post-injection. Later on, the contrast change was no longer present, indicating that the NPs were eliminated within the period of 2-24 hours post-injection. In contrast, in the tumor and brain, no contrast change was visible, suggesting that no NP uptake took place in these tissues (brain images not shown). In the tumor and brain, the MSME-T_2-map showed no significant changes in T_2 times for the different time points (data not shown). In the liver T_2 times could not be reliably quantified due to low signal. These results confirmed what we have already observed with 10 nm sized spherical NPs coated with dendrons molecules[44], that dendronized NPs displayed nonspecific uptake by the RES. By attaching glucose on the surface of NPs, no enhanced NPs uptake into the tumor tissue could be observed. The amount of coupled glucose needs to be tuned to ensure a NPs internalization in tumors visible by MRI. Indeed only very low amount of glucose was grafted as an aggregation due to hydrogen interaction or the loss of charge with high density of glucose was observed.
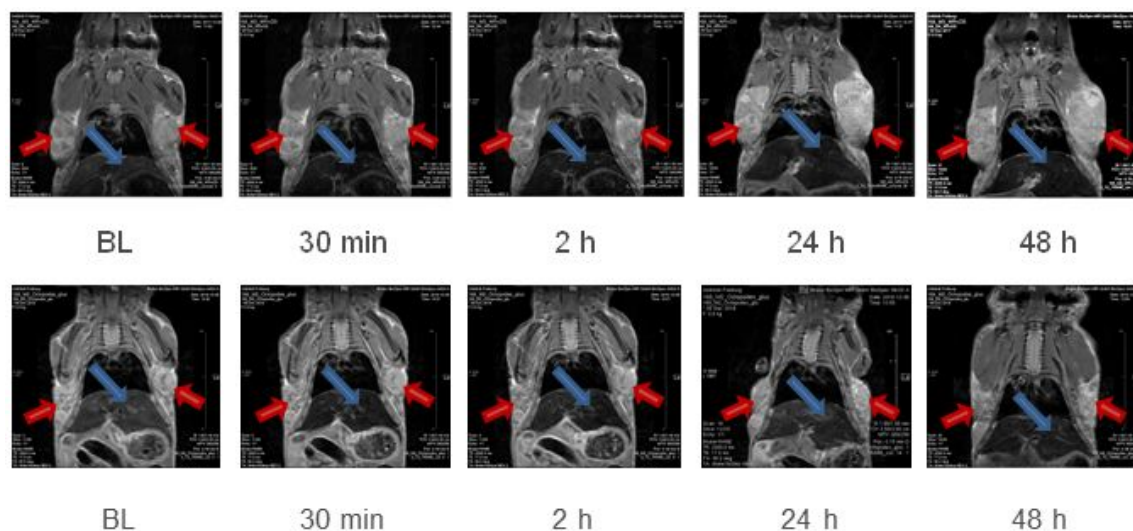
Figure 16. Biodistribution of dendronized octopods NO26 without glucose (upper row) and with glucose coupling (lower row) at different time points over 48 h post-injection. The tumors are pointed out with red arrows and the liver with a blue arrow.
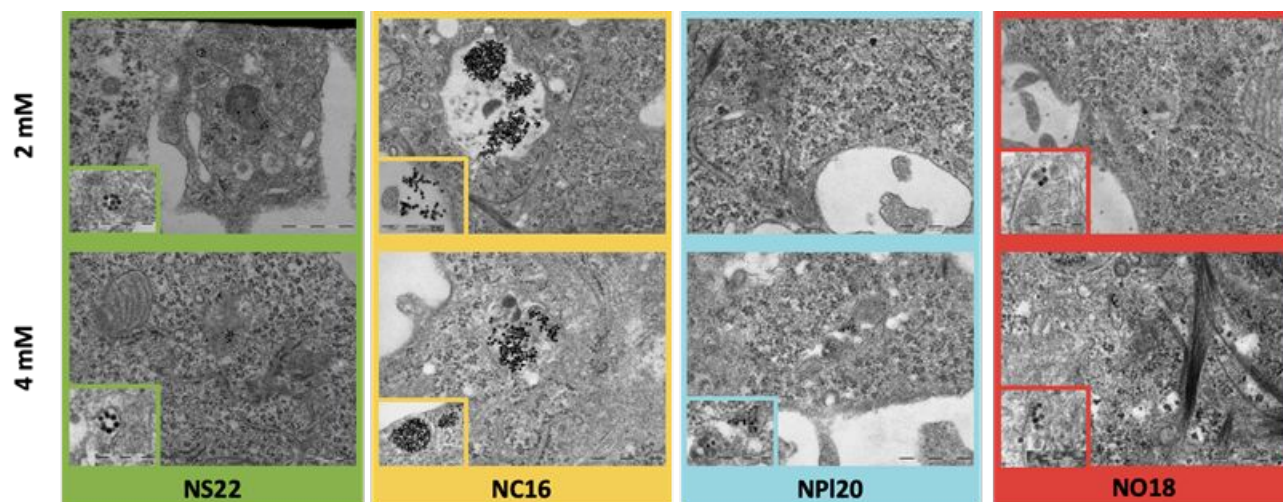
Figure 17. TEM images of internalized cells as a function of the concentration. Inserts present a zoom of NPs inside the cells.

3.4.2 Cell internalization studies and in vitro magnetic hyperthermia with octopods

Cytotoxicity tests demonstrated no toxicity in all NPs up to 8 mM (Figure S17). TEM imaging of cells after incubation with NPs at different concentrations (2 and 4 mM) were performed and results are shown in Figure 17.

For NS18, NS22, NO18 and NPl20, the population of NPs inside phagosomes is low at both tested concentrations. in addition, some local organization has been observed depending on the shape. NS22 tended to form rings, whereas NO18 preferred to align, and NPl20 did not present any sign of local organization. A higher cell internalization was observed with NC16 which may be explained by their aggregation tendency due to their weaker colloidal stability related to their more difficult dendronization. Such aggregation should favor sedimentation of the NPs and hence their contact with the cell monolayer at the bottom of the culture wall: an internalization due to a "weight" effect may thus have been favored as already observed in earlier studies[43].

The results altogether, demonstrated a weak internalization, which is attributed to dendron molecules preventing NPs from non-specific internalization.

In vitro magnetic hyperthermia was carried out with NO18 octopods. In order to achieve a homogeneous exposure of the cell monolayer to the AC field, a bespoke sample holder was designed to accommodate a 10 mm cover slide in a reservoir of complete media. The holder was designed to fit into the environmental chamber designed by nB nanoscale biomagnetics (cf. Experimental conditions). Cell monolayers loaded with NO18 (4mM) were exposed to the corresponding AC field for 1 h and then returned to culture to study the time-dependent response to the treatment. Control experiments without magnetic NPs can be found in Figure S18. Field amplitude and frequency conditions were chosen to mimic the settings used for SAR evaluation. Two conditions were selected, with relative high frequency/low field and low frequency/high field combinations, but very similar *Hxf* factor (even if it is slightly higher than the Hxf factor recommended for clinical trials: 5.10^9 A/m.s[70]).
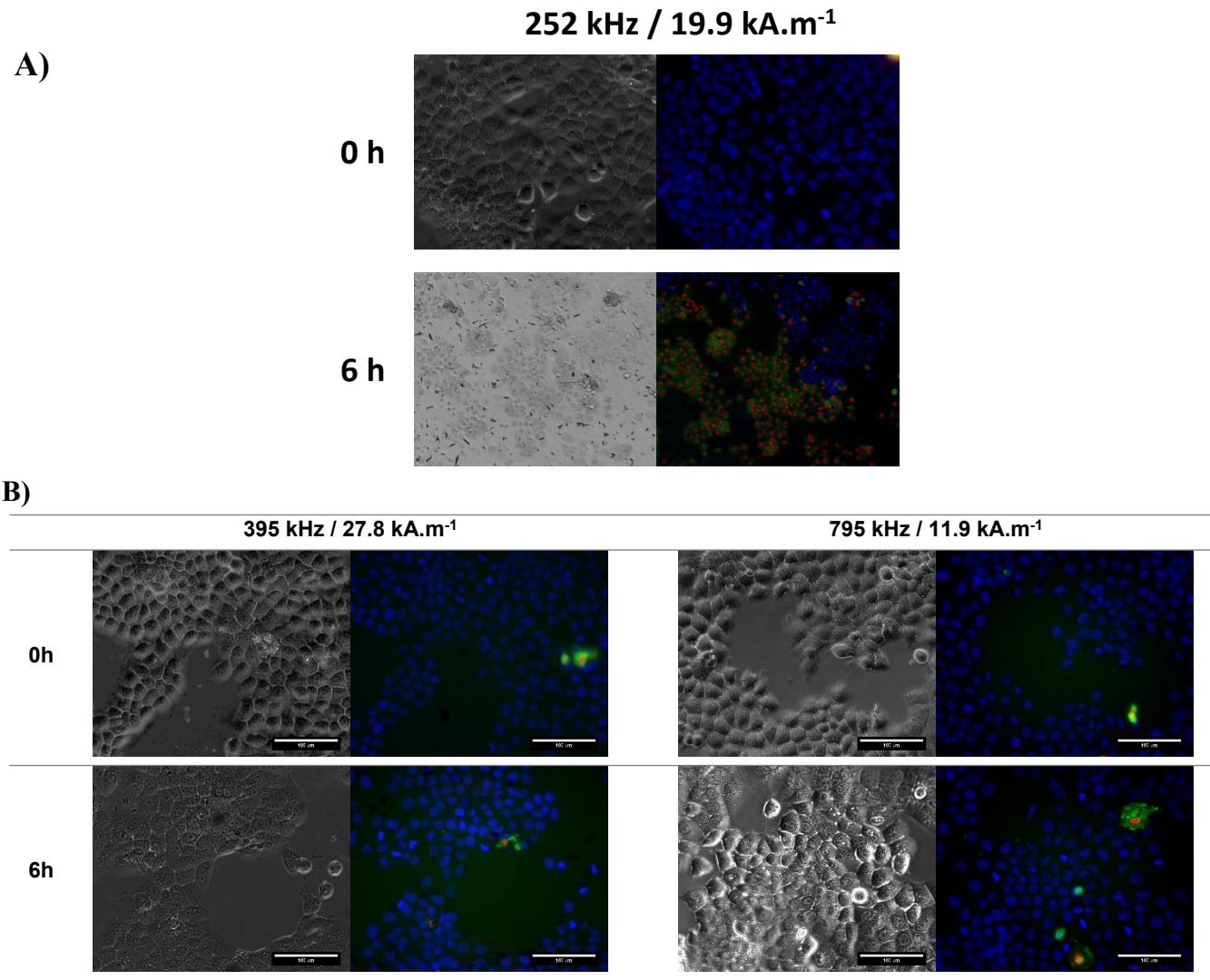
When cells were exposed to 395 kHz and 27.8 kA.m^{-1} for 1 h, no significant cell death was observed just after the MH treatment at t=0 (no effect of possible Eddy currents) and only a marginal increase was seen 6 h after the MH treatment (Figure 18 B). A similar trend was observed when cells were exposed to 795 kHz and 11.9 kA.m^{-1} for 1h. However, cell death was significantly increased at 24 h after MH treatment (Figure 18B). Even though the difference in the *Hxf* factor was very small, cell death was significantly higher when a lower frequency and higher magnetic field amplitude were used. A quantitative evaluation of the cell response is very difficult as cells quickly formed aggregates and floaters upon cell death, yielding unreliable cell counting. Nevertheless, despite a low NPs internalisation, a cell death reaching ca. 50% was estimated in that case, whereas, 20-30% was observed under a higher frequency.

Based on the observed results at lower frequency, a third experiment series was carried out at a more reduced frequency. When cells were exposed to 252 kHz and 19.9 kA.m^{-1} for 1 h, a rapid uneven response was observed (Figure 18.A). Rapid formation of cell aggregates and floaters were observed in some areas, whereas, other cells were completely unaffected. At 6 h, more than ca. 60% of the cells were labelled as dead forming big aggregates and detaching. It was not possible to image at 24 h as all cells were dead floating. These *in vitro* experiments confirmed the good magnetic heating properties of octopods for magnetic hyperthermia especially at low frequency.

3.4.3 in vivo magnetic hyperthermia

To further check the *in vivo* magnetic hyperthermia properties of dendronized octopods, NO26 were injected intratumoraly in mice as they do not internalize unspecifically in a high amount. These preliminary experiments detailed in SI (Figure S19a) showed no effects in tumour inhibition growth. PERLS staining performed in order to detect NO26 in tissue sections (Figure S19b-c) evidenced that NPs are mainly in the extracellular matrix, even if some can be detected in the tumor. NO26 NPs were very stable and easy to inject, but the main problem is that they stayed in the extracellular matrix instead of being internalized in the tumor. That would confirm again that dendron coating prevents NPs from unspecific internalization[44,54].

252 kHz / 19.9 kA.m^{-1}

A) 0 h, 6 h

B)

**395 kHz / 27.8 kA.m^{-1}**   **795 kHz / 11.9 kA.m^{-1}**

0h, 6h
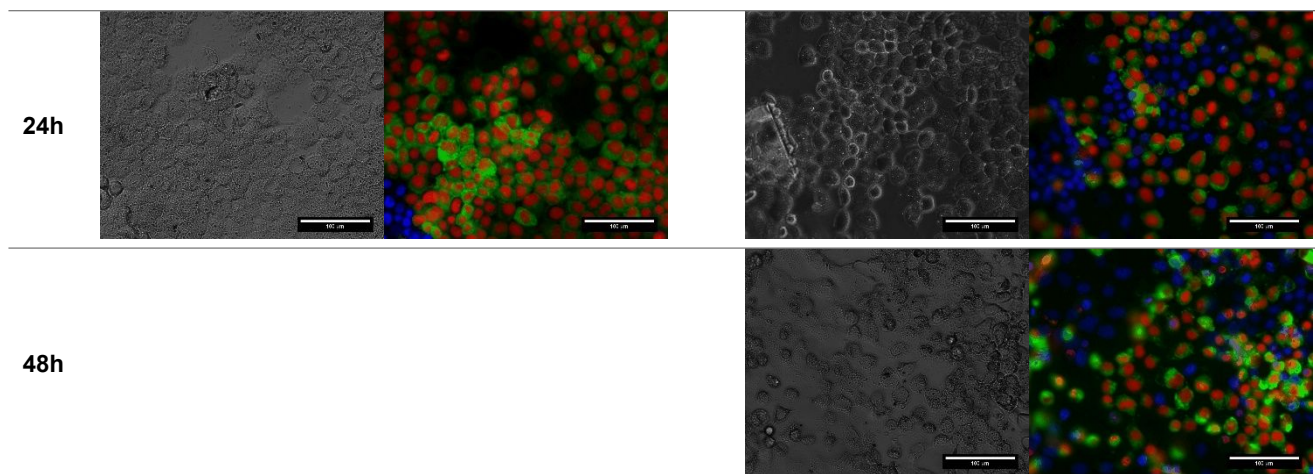
Figure 18. Huh-7 cells loaded with 4mM NO18 exposed to 252 kHz and 19.9 kA.m-1 at A) t=0h and 6h after 1h treatment. B) Huh-7 cells loaded with NO18 (4 mM) exposed to 395 kHz and 27.8 kA.m-1 (left panel) at a-b) t=0h, c-d) 6h and e-h) 24h after 1h treatment and at 795 kHz and 11.9 kA.m-1 (right panel) at a-b) t=0h, c-d) 6h, e-f) 24h and g-h) 48h after 1h treatment. Cells were labeled with Annexin V-FITC (green), PI (red) and hoechst (blue).

In order to evidence an *in vivo* hyperthermia effect of octopods, further experiments have been performed by coupling glucose at the surface of dendronized NPs (by using the carboxylate function of dendrons) to improve their internalization in tumoral cells. The results given in Figure 19 show that the coupling of a small amount of glucose succeeded in showing an effect of MH on the tumor growth.
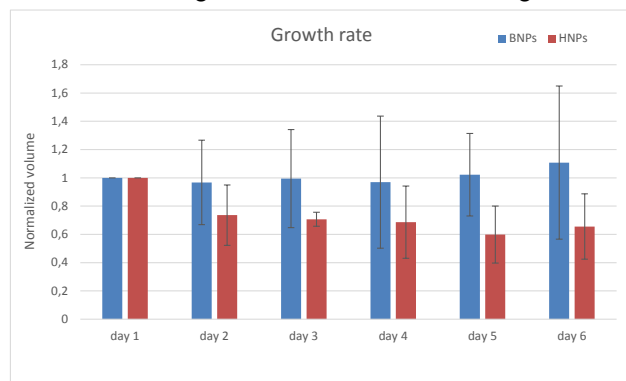
Figure 19. Tumour growth with NO26 NPs coupled with small amount of glucose without (blue color) and with (red color) magnetic field exposure.

3.5 Discussion

By investigating the synthesis of NPs with different shapes using home-made iron stearates precursors, we succeeded in synthesizing NPs with different shapes[25,51] (nanoplates, nanocubes and octopods) and in evaluating their MRI and magnetic hyperthermia properties after their coating with dendron molecules. Nanospheres were also included as isotropic nano-objects. The NPs have all been coated with dendrons molecules and the dendronization step had to be adapted to each shape. The dendronization was more difficult with nanocubes which were ultimately more agregated than other shaped NPs.

Cell internalization experiments with all dendronized shaped NPs and in vivo experiments with dendronized octopods have confirmed again the antifouling properties ensured by the dendron coating which also allow, by its small size, a mean hydrodynamic size smaller than 100 nm. The dendron efficiency is thus ensured whatever the size and shape of NPs and the dendron coating provides high colloidal stability, relaxivity values (water diffusion around the magnetic core) and biocompatibility. Nevertheless, this performance needs a strong master of the functionnalization step which should ensure a quite full ligand exchange with hydrophobic surfactants. Yet, oleic acid (OA) can change the interaction with cell surface and elicit passive membrane translocation by direct interaction of OA with the fatty acids compounds of the extracellular membrane: this has been attributed to the higher disrupting nature of the kinked chain of these fatty acids that would result in higher magnitude of lipid disruption thus leading to increased cellular uptake [71, and references therein]. But, we recently showed that a dendritic biphosphonic tweezer anchoring at the surface of NPs drastically lowers the amount of OA remaining at the NP surface after the ligand exchange process[44]. Furthermore previously reported studies showed that endocytosis is the main mechanism of cellular internalization of magnetic NPs[72]. Yet, dendritic phosphonates strongly stabilize magnetic NPs through electrosteric interactions, thus preventing the formation of aggregates[43,73,74] Thus, by preventing the aggregate formation, but also by reducing the amount of OA surfactant present on the NPs surface, a dendritic coating through a biphosphonic acid allows extremely effective reduction of unspecific cellular uptake, as already shown in various cancer cell lines[44].

Among all investigated shaped NPs, dendronized octopods were the NPs which exhibited the highest promises for combining therapy by magnetic hyperthermia and as contrast agent for MRI. That was confirmed by MH on cells which evidenced also a higher effect at low frequency. The biodistribution investigation by MRI demonstrated again the antifouling properties provided by the dendron coating which has needed to couple glucose on dendronized octopods to be able to observe an effect of MH on tumor growth.

Besides octopods, nanospheres display interesting relaxivities and SAR values when their size is larger than 18 nm. Nanoplates and nanocubes presented interesting properties as contrast agent for MRI but lower SAR values.

To better understand what are the main characteristics of octopods and nanospheres, by comparison with nanoplates and nanocubes, which can explain their higher properties, the

structural and magnetic properties of the different NPs have been investigated by different techniques.

XRD and IR spectroscopy characterizations techniques showed that all shaped NPs except nanocubes consist in oxidized magnetite before dendronization. After the dendronization step of NPs, Mössbauer data and earlier studies allowed reporting that the core of the spheres consists of magnetite covered by maghemite, while the other octopod- and nanoplate-shaped ones probably result from a rather continuous distribution of oxidation states ranging from ferric to intermediate ferric-ferrous-state. TEM-EELS analysis showed that the surface of octopods and nanoplates would contain some lower valence state iron cations. Mössbauer under an applied field showed that for nanospheres, only iron in octahedral sites are canted and on a very small thickness in agreement with earlier studies[31]. By contrast, the canting in octopods affects iron on both sites and on a larger thickness. Possible explanation to the peticular surface composition of octopods and nanoplates could be this canting or the growth process of such anisotropic shape which may be due to the growth of a $Fe_{1-x}O$ phase which oxidizes or a phosphonatation during the dendronization which occurs differently from that observed usually with isotropic shapes. Indeed phosphate iron II phases exist such as iron II phosphate ($Fe_3(PO_4)_2$) and iron II dihydrogen phosphate $Fe(H_2PO_4)_2$ and a different anchoring of phosphonate from dendron at the surface of such complex surface would be possible.

Shape anisotroy does not contribute towards an improved nanoparticle heating in the case of nanoplates. It may be related to their composition close to that of maghemite but also to a more perturbated structure. Indeed, TEM EELS measurement suggested a reduced valence of Fe at the surface by comparison with the core. ZFC/FC measurement showed the presence of a peak related to a spin-glass-like behavior of the superficial spins when Mössbauer spectroscopy under an applied field evidenced no spin canting confirmed by the low exchange bias field deduced from FC measurements. In addition, nanoplates exhibited the highest Hc_0 values among all shapes (Table S1). These features may be related to the small thickness of nanoplates which affect their internal structure. Our future works will aim at better mastering the growth of nanoplates.

Concerning Hc values, the correlation here observed between H_C and SAR values in Table S1 confirms the recent suggestion made by Starsich et al.[75], which states that coercivity values determine the heating capabilities of nanoparticles. More specifically, samples showing lower coercivity values or larger saturation magnetization σ_S to H_C ratios also present a better heating efficiency. In fact, the best 'heater' of the series is sample NO18, which shows both the lowest H_C.

The comparison of relaxivities and SAR values demonstrated that nanospheres combine also very good MRI and MH properties which increase with their diameter when the opposite is observed with octopods with the smallest size exhibiting the highest performance.

The case of nanosphere is quite simple as we have already demonstrated that the composition get closer to the magnetite one with the increase of their size as well as their saturation magnetisation. All the characterization performed here after the dendronisation step confirmed this evolution and especially the intenser peak corresponding to the Verwey transition in ZFC/FC curves for NS22 by comparison with NS18. The dependency of relaxivity and SAR values with size could be easily explained by the enhanced magnetic properties with the size increase (and the observation by Smolensky et al[76]). However, the Neel mechanism is identified as the main heating mechanism when normally in this range of sizes, the Brownian motion should highly contribute[8]. We explain such behavior by the presence of volume defects inside nanospheres. These defects were evidenced by crystallite size measurements from XRD pattern and HRTEM and confirmed by the high coercive field of the NPs despite their isotropic shape. That is in agreement with recent results of Pellegrino et al[53] who have investigated the MH properties of core-shell wustite@spinel nanocubes at different oxidation steps. Thus, the presence of defects does not affect their magnetic hyperthermia properties and even contribute to them by favoring the Neel relaxation.

Octopods exhibited the highest performances for MRI and MH clearly related to their shape anisotropy. It has already been demonstrated that relaxivity values can be optimized by varying NP shape[76–78]. This was observed by Joshi et al[78] and Smolenski et al.[76] when they compared spherical and faceted NPs, leading in both cases to higher values of relaxivity for faceted NPs. Similarly, cubic spinel iron oxide NPs ($r_2 = 761$ $mM^{-1}·s^{-1}$ at 3 T)[79], as well as octopod IONPs (edge length of 30 nm) ($r_2 = 679.3 \pm 30$ $mM^{-1}.s^{-1}$ at 7 T) exhibited significant transverse relaxivity values[22,24]. The high relaxivity values measured in octopod NPs are due to the modified symmetry of the stray field gradients around their elongated edges, causing a change in the diffusion of surrounding water protons. The extent of the stray field gradient dictates the degree of phase coherence loss of protons –the larger r_2 values - when circulating close to the octopods.

Surface effects are also evidenced such as spin canting and an oxidation degree of iron which varies along with the faces (EELS studies). Nevertheless, this effect seems to depend on the size with a stronger effect for small sized octopods (relaxivity and SAR measurements). The peak P4 in Figure 5 corresponding to surface spin glass is very intense for NO18 by comparison with NO26. The concave faces along elongated corners at the nanoscale make that several iron planes are exhibited at the surface which is confirmed by the spin canting with spheres only observed in Oh sites when both iron sites are canted with octopods. This complex surface should affect their whole magnetic properties, but the octopods performance is mainly related to their shape anisotropy which should induce locally heterogeneous magnetic field suitable for MRI and MH. Zhou et al[80] reported that magnetic field inhomogeneity induced by clustering or shape of NPs are favorable to enhance T_2 relaxivity.

Nanoparticle heating depends on the total anisotropy: we explain the anisotropy enhancement effect supported by theoretical calculations (see supplementary information). Calculated shape anisotropy values for octopods (see ESI) support the proposed role of nanoparticle shape in increasing the anisotropy field and hence the effective field "felt" by NPs. The obtained theoretical total anisotropy values considering both shape and surface effects on octopod

nanoparticles amount to 78.7 kJ/m³, in the same order of magnitude but well above than that of bulk magnetite (-13.5 kJ/m³)[81]. This is translated in a more intense modification of the diffusion of water molecules around NPs. Sample NO18 presented a larger T2 value than NO26. Considering a similar shape anisotropy contribution from both samples, it is reasonable to ascribe this difference to a tip (elongated corner) effect more important for NO18 than for NO26. Indeed the tip/corner represents a higher part of the volume for NO18 and may introduce a higher local magnetic heterogeneity favorable for enhancing the relaxivity[80]. Such tip effects on the magnetic field inhomogeneity account for the unusual NMRD profile and TEM-EELS results.

The AC hysteresis analysis reveal that the bigger octopods NO26 may present a performance reduction in vitro and in vivo due to the prevalent Brownian heating mechanism. The higher viscosity of bodily fluids and tissues will affect the mechanical contribution from the brownian relaxation to the magnetomechanical torque behind nanoparticle heating processes. The rest of the samples are much less prone to be affected by the medium viscosity and hence their performance should remain unaltered in biological media.

4. Conclusion

NPs with different shapes (nanosphere, nanocube, nanoplate and octopod) have been synthesized from *home made* precursors and coated with dendron molecules displaying an arborescent architecture. The small size and the design of the dendron with two phosphonate groups as anchoring groups at the surface of NPs and with three PEG chains at the periphery has been shown again efficient, through *in vitro* and *in vivo* experiments, to ensure antifouling properties to NPs whatever their size and shape. The design of the dendron allowed to improve the ligand exchange process and to limit the amount of remaining oleic acid which favors cell internalisation.

Among all shaped nanoparticles, dendronized nanospheres and octopods were shown to exhibit both high MRI and MH performances.

The NPs have been characterized by different techniques such as Mössbauer spectroscopy under an applied field, HRTEM EELS, determination of NMRD profiles. Even if nanoplates were expected to display shape anisotropy, their magnetic properties are low due to their thickness affecting strongly their crystallinity and surface properties. Nanocubes were difficult to coat with dendron molecules due to their flat faces coated with a strongly interacting oleic acid monolayer rendering difficult the ligand exchange by dendron molecules. Their composition consisting in a core-shell wustite@spinel iron oxide and their higher aggregation state led to good MRI contrast agent properties but weakened their magnetic hyperthermia performance.

Octopods and nanospheres were shown to exhibit the larger relaxivity and heating values. Nanospheres display a spinel composition but present a lot of internal defects which seem to enhance their magnetic hyperthermia and MRI performances. Indeed, they display high coercive fields and their heating properties are mainly due to the Neel relaxation which is required when internalized in cells. The exceptional properties of octopods were further studied by some *in vitro* and *in vivo* experiments. The different characterization evidenced a complex surface state and composition due to their concave shape with elongated corners but also a clear shape anisotropy favorable to imaging by MRI and magnetic hyperthermia.

Their shape with tips effects induces magnetic field inhomogeneity which may also explain the unusual NMRD profile and TEM-EELS results. Octopods with a mean size around 20 nm are required to ensure a MH heating by Neel relaxation as larger size favour a brownian relaxation.

In conclusion, nanospheres with mean size higher than 20 nm and containing defects preserving the Neel relaxation for magnetic hyperthemia as well as octopods with mean size around 20 nm to avoid Brownian relaxation are promising nano-objects for theranostics. For enhanced cell-specific NP uptake a suitable targeting ligands might be attached to the surface of these dendronized iron oxide NPs.

ASSOCIATED CONTENT

Supporting Information is available. This material is available free of charge via the Internet at http://pubs.acs.org.

AUTHOR INFORMATION

Corresponding Author

* Prof. S. Begin-Colin*
Université de Strasbourg, CNRS, Institut de Physique et Chimie des Matériaux de Strasbourg, UMR 7504, F-67034 Strasbourg, France
E-mail : sylvie.begin@unistra.fr

Author Contributions

All authors have given approval to the final version of the manuscript.

REFERENCES

(1) Liong, M.; Lu, J.; Kovochich, M.; Xia, T.; Ruehm, S. G.; Nel, A. E.; Tamanoi, F.; Zink, J. I. Multifunctional Inorganic Nanoparticles for Imaging, Targeting, and Drug Delivery. *ACS Nano* **2008**, *2* (5), 889–896. https://doi.org/10.1021/nn800072t.

(2) Kim, J.; Piao, Y.; Hyeon, T. Multifunctional Nanostructured Materials for Multimodal Imaging, and Simultaneous Imaging and Therapy. *Chem. Soc. Rev.* **2009**, *38* (2), 372–390. https://doi.org/10.1039/B709883A.

(3) De, M.; Ghosh, P. S.; Rotello, V. M. Applications of Nanoparticles in Biology. *Adv. Mater.* **2008**, *20* (22), 4225–4241. https://doi.org/10.1002/adma.200703183.

(4) Mornet, S.; Vasseur, S.; Grasset, F.; Duguet, E. Magnetic Nanoparticle Design for Medical Diagnosis and Therapy. *J. Mater. Chem.* **2004**, *14* (14), 2161–2175. https://doi.org/10.1039/B402025A.

(5) Yoo, D.; Lee, J.-H.; Shin, T.-H.; Cheon, J. Theranostic Magnetic Nanoparticles. *Acc. Chem. Res.* **2011**, *44* (10), 863–874. https://doi.org/10.1021/ar200085c.

(6) Fang, C.; Zhang, M. Multifunctional Magnetic Nanoparticles for Medical Imaging Applications. *J Mater Chem* **2009**, *19*, 6258–6266. https://doi.org/10.1039/b902182e.

(7) Laurent, S.; Forge, D.; Port, M.; Roch, A.; Robic, C.; Vander Elst, L.; Muller, R. N. Magnetic Iron Oxide Nanoparticles: Synthesis, Stabilization, Vectorization, Physicochemical Characterizations, and Biological Applications. *Chem. Rev.* **2008**, *108* (6), 2064–2110. https://doi.org/10.1021/cr068445e.

(8) Blanco-Andujar, C.; Walter, A.; Cotin, G.; Bordeianu, C.; Mertz, D.; Felder-Flesch, D.; Begin-Colin, S. Design of Iron Oxide-Based Nanoparticles for MRI and Magnetic Hyperthermia. *Nanomedicine (Lond)* **2016**, *11* (14), 1889–1910. https://doi.org/10.2217/nnm-2016-5001.

(9) Gazeau, F.; Lévy, M.; Wilhelm, C. Optimizing Magnetic Nanoparticle Design for Nanothermotherapy. *Nanomedicine (Lond)* **2008**, *3* (6), 831–844. https://doi.org/10.2217/17435889.3.6.831.

(10) Maier-Hauff, K.; Rothe, R.; Scholz, R.; Gneveckow, U.; Wust, P.; Thiesen, B.; Feussner, A.; Deimling, A. von; Waldoefner, N.; Felix, R.; et al. Intracranial Thermotherapy Using Magnetic Nanoparticles Combined with External Beam Radiotherapy: Results of a Feasibility Study on Patients with Glioblastoma Multiforme. *J Neurooncol* **2007**, *81* (1), 53–60. https://doi.org/10.1007/s11060-006-9195-0.

(11) Maier-Hauff, K.; Ulrich, F.; Nestler, D.; Niehoff, H.; Wust, P.; Thiesen, B.; Orawa, H.; Budach, V.; Jordan, A. Efficacy and Safety of Intratumoral Thermotherapy Using Magnetic Iron-Oxide Nanoparticles Combined with External Beam Radiotherapy on Patients with Recurrent Glioblastoma Multiforme. *J Neurooncol* **2011**, *103* (2), 317–324. https://doi.org/10.1007/s11060-010-0389-0.

(12) Http://Www.Magforce.de/En/Home.Html.

(13) Germany: Investment Plan for Europe - EIB backs cancer therapy developer MagForce with up to EUR 35m http://www.eib.org/infocentre/press/releases/all/2017/2017-221-investment-plan-for-europe-eib-backs-german-cancer-therapy-developer-magforce-with-up-to-eur-35m.htm (accessed Feb 21, 2019).

(14) Deatsch, A. E.; Evans, B. A. Heating Efficiency in Magnetic Nanoparticle Hyperthermia. *Journal of Magnetism and Magnetic Materials* **2014**, *354*, 163–172. https://doi.org/10.1016/j.jmmm.2013.11.006.

(15) Kolosnjaj-Tabi, J.; Di Corato, R.; Lartigue, L.; Marangon, I.; Guardia, P.; Silva, A. K. A.; Luciani, N.; Clément, O.; Flaud, P.; Singh, J. V.; et al. Heat-Generating Iron Oxide Nanocubes: Subtle "Destructurators" of the Tumoral Microenvironment. *ACS Nano* **2014**, *8* (5), 4268–4283. https://doi.org/10.1021/nn405356r.

(16) Daou, T. J.; Pourroy, G.; Bégin-Colin, S.; Grenèche, J. M.; Ulhaq-Bouillet, C.; Legaré, P.; Bernhardt, P.; Leuvrey, C.; Rogez, G. Hydrothermal Synthesis of Monodisperse Magnetite Nanoparticles. *Chemistry of Materials* **2006**, *18* (18), 4399–4404. https://doi.org/10.1021/cm060805r.

(17) Santoyo Salazar, J.; Perez, L.; de Abril, O.; Truong Phuoc, L.; Ihiawakrim, D.; Vazquez, M.; Greneche, J.-M.; Begin-Colin, S.; Pourroy, G. Magnetic Iron Oxide Nanoparticles in 10−40 Nm Range: Composition in Terms of Magnetite/Maghemite Ratio and Effect on the Magnetic Properties. *Chem. Mater.* **2011**, *23* (6), 1379–1386. https://doi.org/10.1021/cm103188a.

(18) Basly, B.; Popa, G.; Fleutot, S.; Pichon, B. P.; Garofalo, A.; Ghobril, C.; Billotey, C.; Berniard, A.; Bonazza, P.; Martinez, H.; et al. Effect of the Nanoparticle Synthesis Method on Dendronized Iron Oxides as MRI Contrast Agents. *Dalton Trans.* **2013**, *42* (6), 2146–2157. https://doi.org/10.1039/C2DT31788E.

(19) Guardia, P.; Di Corato, R.; Lartigue, L.; Wilhelm, C.; Espinosa, A.; Garcia-Hernandez, M.; Gazeau, F.; Manna, L.; Pellegrino, T. Water-Soluble Iron Oxide Nanocubes with High Values of Specific Absorption Rate for Cancer Cell Hyperthermia Treatment. *ACS Nano* **2012**, *6* (4), 3080–3091. https://doi.org/10.1021/nn2048137.

(20) Lartigue, L.; Hugounenq, P.; Alloyeau, D.; Clarke, S. P.; Lévy, M.; Bacri, J.-C.; Bazzi, R.; Brougham, D. F.; Wilhelm, C.; Gazeau, F. Cooperative Organization in Iron Oxide Multi-Core Nanoparticles Potentiates Their Efficiency as Heating Mediators and MRI Contrast Agents. *ACS Nano* **2012**, 121129155806007. https://doi.org/10.1021/nn304477s.

(21) Nemati, Z.; Alonso, J.; Martinez, L. M.; Khurshid, H.; Garaio, E.; Garcia, J. A.; Phan, M. H.; Srikanth, H. Enhanced Magnetic Hyperthermia in Iron Oxide Nano-Octopods: Size and Anisotropy Effects. *The Journal of Physical Chemistry C* **2016**, *120* (15), 8370–8379. https://doi.org/10.1021/acs.jpcc.6b01426.

(22) Zhao, Z.; Zhou, Z.; Bao, J.; Wang, Z.; Hu, J.; Chi, X.; Ni, K.; Wang, R.; Chen, X.; Chen, Z.; et al. Octapod Iron Oxide Nanoparticles as High-Performance T2 Contrast Agents for Magnetic Resonance Imaging. *Nat Commun* **2013**, *4*, 2266. https://doi.org/10.1038/ncomms3266.

(23) Kumar, C. S. S. R.; Mohammad, F. Magnetic Nanomaterials for Hyperthermia-Based Therapy and Controlled Drug Delivery. *Advanced Drug Delivery Reviews* **2011**, *63* (9), 789–808. https://doi.org/10.1016/j.addr.2011.03.008.

(24) Sathya, A.; Guardia, P.; Brescia, R.; Silvestri, N.; Pugliese, G.; Nitti, S.; Manna, L.; Pellegrino, T. CoxFe3–XO4 Nanocubes for Theranostic Applications: Effect of Cobalt Content and Particle Size. *Chem. Mater.* **2016**, *28* (6), 1769–1780. https://doi.org/10.1021/acs.chemmater.5b04780.

(25) Cotin, G.; Kiefer, C.; Perton, F.; Ihiawakrim, D.; Blanco-Andujar, C.; Moldovan, S.; Lefevre, C.; Ersen, O.; Pichon, B.; Mertz, D.; et al. Unravelling the Thermal

Decomposition Parameters for The Synthesis of Anisotropic Iron Oxide Nanoparticles. *Nanomaterials* **2018**, *8* (11), 881. https://doi.org/10.3390/nano8110881.

(26) Palchoudhury, S.; Xu, Y.; Rushdi, A.; Holler, R. A.; Bao, Y. Controlled Synthesis of Iron Oxide Nanoplates and Nanoflowers. *Chemical Communications* **2012**, *48* (85), 10499. https://doi.org/10.1039/c2cc35945f.

(27) Palchoudhury, S.; An, W.; Xu, Y.; Qin, Y.; Zhang, Z.; Chopra, N.; Holler, R. A.; Turner, C. H.; Bao, Y. Synthesis and Growth Mechanism of Iron Oxide Nanowhiskers. *Nano Letters* **2011**, *11* (3), 1141–1146. https://doi.org/10.1021/nl200136j.

(28) Kovalenko, M. V.; Bodnarchuk, M. I.; Lechner, R. T.; Hesser, G.; Schäffler, F.; Heiss, W. Fatty Acid Salts as Stabilizers in Size- and Shape-Controlled Nanocrystal Synthesis: The Case of Inverse Spinel Iron Oxide. *J. Am. Chem. Soc.* **2007**, *129* (20), 6352–6353. https://doi.org/10.1021/ja0692478.

(29) Shavel, A.; Rodríguez-González, B.; Pacifico, J.; Spasova, M.; Farle, M.; Liz-Marzán, L. M. Shape Control in Iron Oxide Nanocrystal Synthesis, Induced by Trioctylammonium Ions. *Chemistry of Materials* **2009**, *21* (7), 1326–1332. https://doi.org/10.1021/cm803201p.

(30) Noh, S.; Na, W.; Jang, J.; Lee, J.-H.; Lee, E. J.; Moon, S. H.; Lim, Y.; Shin, J.-S.; Cheon, J. Nanoscale Magnetism Control via Surface and Exchange Anisotropy for Optimized Ferrimagnetic Hysteresis. *Nano Letters* **2012**, *12* (7), 3716–3721. https://doi.org/10.1021/nl301499u.

(31) Baaziz, W.; Pichon, B. P.; Fleutot, S.; Liu, Y.; Lefevre, C.; Greneche, J.-M.; Toumi, M.; Mhiri, T.; Begin-Colin, S. Magnetic Iron Oxide Nanoparticles: Reproducible Tuning of the Size and Nanosized-Dependent Composition, Defects, and Spin Canting. *J. Phys. Chem. C* **2014**, *118* (7), 3795–3810. https://doi.org/10.1021/jp411481p.

(32) Zhou, Z.; Zhao, Z.; Zhang, H.; Wang, Z.; Chen, X.; Wang, R.; Chen, Z.; Gao, J. Interplay between Longitudinal and Transverse Contrasts in Fe3O4 Nanoplates with (111) Exposed Surfaces. *ACS Nano* **2014**, *8* (8), 7976–7985. https://doi.org/10.1021/nn5038652.

(33) Thanh, N. T. *Magnetic Nanoparticles: From Fabrication to Clinical Applications*; CRC Press: Boca Raton, FL, 2012.

(34) Rolland, O.; Turrin, C.-O.; Caminade, A.-M.; Majoral, J.-P. Dendrimers and Nanomedicine: Multivalency in Action. *New J. Chem.* **2009**, *33* (9), 1809–1824. https://doi.org/10.1039/B901054H.

(35) Cloninger, M. J. Biological Applications of Dendrimers. *Current Opinion in Chemical Biology* **2002**, *6* (6), 742–748. https://doi.org/10.1016/S1367-5931(02)00400-3.

(36) Stiriba, S.-E.; Frey, H.; Haag, R. Dendritic Polymers in Biomedical Applications: From Potential to Clinical Use in Diagnostics and Therapy. *Angew. Chem. Int. Ed. Engl.* **2002**, *41* (8), 1329–1334.

(37) Duncan, R.; Izzo, L. Dendrimer Biocompatibility and Toxicity. *Adv. Drug Deliv. Rev.* **2005**, *57* (15), 2215–2237. https://doi.org/10.1016/j.addr.2005.09.019.

(38) Ghobril, C.; Popa, G.; Parat, A.; Billotey, C.; Taleb, J.; Bonazza, P.; Begin-Colin, S.; Felder-Flesch, D. A Bisphosphonate Tweezers and Clickable PEGylated PAMAM Dendrons for the Preparation of Functional Iron Oxide Nanoparticles Displaying Renal and Hepatobiliary Elimination. *Chem. Commun. (Camb.)* **2013**, *49* (80), 9158–9160. https://doi.org/10.1039/c3cc43161d.

(39) Basly, B.; Felder-Flesch, D.; Perriat, P.; Billotey, C.; Taleb, J.; Pourroy, G.; Begin-Colin, S. Dendronized Iron Oxide Nanoparticles as Contrast Agents for MRI. *Chem. Commun.* **2010**, *46* (6), 985–987. https://doi.org/10.1039/B920348F.

(40) Lamanna, G.; Kueny-Stotz, M.; Mamlouk-Chaouachi, H.; Ghobril, C.; Basly, B.; Bertin, A.; Miladi, I.; Billotey, C.; Pourroy, G.; Begin-Colin, S.; et al. Dendronized Iron Oxide Nanoparticles for Multimodal Imaging. *Biomaterials* **2011**, *32* (33), 8562–8573. https://doi.org/10.1016/j.biomaterials.2011.07.026.

(41) Chevallier, P.; Walter, A.; Garofalo, A.; Veksler, I.; Lagueux, J.; Bégin-Colin, S.; Felder-Flesch, D.; Fortin, M.-A. Tailored Biological Retention and Efficient Clearance of Pegylated Ultra-Small MnO Nanoparticles as Positive MRI Contrast Agents for Molecular Imaging. *Journal of Materials Chemistry B* **2014**, *2* (13), 1779. https://doi.org/10.1039/c3tb21634a.

(42) Walter, A.; Billotey, C.; Garofalo, A.; Ulhaq-Bouillet, C.; Lefèvre, C.; Taleb, J.; Laurent, S.; Vander Elst, L.; Muller, R. N.; Lartigue, L.; et al. Mastering the Shape and Composition of Dendronized Iron Oxide Nanoparticles To Tailor Magnetic Resonance Imaging and Hyperthermia. *Chem. Mater.* **2014**, *26* (18), 5252–5264. https://doi.org/10.1021/cm5019025.

(43) Walter, A.; Garofalo, A.; Bonazza, P.; Meyer, F.; Martinez, H.; Fleutot, S.; Billotey, C.; Taleb, J.; Felder-Flesch, D.; Begin-Colin, S. Effect of the Functionalization Process on the Colloidal, Magnetic Resonance Imaging, and Bioelimination Properties of Mono- or Bisphosphonate-Anchored Dendronized Iron Oxide Nanoparticles. *ChemPlusChem* **2017**, *82* (4), 647–659. https://doi.org/10.1002/cplu.201700049.

(44) Bordeianu, C.; Parat, A.; Affolter-Zbaraszczuk, C.; Muller, R. N.; Boutry, S.; Begin-Colin, S.; Meyer, F.; Laurent, S.; Felder-Flesch, D. How a Grafting Anchor Tailors the Cellular Uptake and in Vivo Fate of Dendronized Iron Oxide Nanoparticles. *J. Mater. Chem. B* **2017**, *5* (26), 5152–5164. https://doi.org/10.1039/C7TB00781G.

(45) Rodríguez-Carvajal, J. Recent Advances in Magnetic Structure Determination by Neutron Powder Diffraction. *Physica B: Condensed Matter* **1993**, *192* (1), 55–69. https://doi.org/10.1016/0921-4526(93)90108-I.

(46) Le Bail, A.; Duroy, H.; Fourquet, J. L. Ab Initio Structure Determination of LiSbWO6 by X Ray Powder Diffraction. *Materials Research Bulletin* **1988**, *23*, 447–452. https://doi.org/10.1016/0025-5408(88)90019-0.

(47) Teillet, J.; Varret, F. Unpublished MOSFIT Program. Université du Maine, Le Mans, France.

(48) Connord, V.; Mehdaoui, B.; Tan, R. P.; Carrey, J.; Respaud, M. An Air-Cooled Litz Wire Coil for Measuring the High Frequency Hysteresis Loops of Magnetic Samples—A Useful Setup for Magnetic Hyperthermia Applications. *Review of Scientific Instruments* **2014**, *85* (9), 093904. https://doi.org/10.1063/1.4895656.

(49) Fabian, K. Approach to Saturation Analysis of Hysteresis Measurements in Rock Magnetism and Evidence for Stress Dominated Magnetic Anisotropy in Young Mid-Ocean Ridge Basalt. *Physics of the Earth and Planetary Interiors* **2006**, *154* (3), 299–307. https://doi.org/10.1016/j.pepi.2005.06.016.

(50) Box, G. E. P.; Lucas, H. L. DESIGN OF EXPERIMENTS IN NON-LINEAR SITUATIONS. *Biometrika* **1959**, *46* (1–2), 77–90. https://doi.org/10.1093/biomet/46.1-2.77.

(51) Cotin, G.; Kiefer, C.; Perton, F.; Boero, M.; Özdamar, B.; Bouzid, A.; Ori, G.; Massobrio, C.; Begin, D.; Pichon, B.; et al. Evaluating the Critical Roles of Precursor Nature and Water Content When Tailoring Magnetic Nanoparticles for Specific Applications. *ACS*

Appl. Nano Mater. **2018**, *1* (8), 4306–4316. https://doi.org/10.1021/acsanm.8b01123.

(52) Pichon, B. P.; Gerber, O.; Lefevre, C.; Florea, I.; Fleutot, S.; Baaziz, W.; Pauly, M.; Ohlmann, M.; Ulhaq, C.; Ersen, O.; et al. Microstructural and Magnetic Investigations of Wüstite-Spinel Core-Shell Cubic-Shaped Nanoparticles. *Chem. Mater.* **2011**, *23* (11), 2886–2900. https://doi.org/10.1021/cm2003319.

(53) Lak, A.; Cassani, M.; Mai, B. T.; Winckelmans, N.; Cabrera, D.; Sadrollahi, E.; Marras, S.; Remmer, H.; Fiorito, S.; Cremades-Jimeno, L.; et al. Fe2+ Deficiencies, FeO Subdomains, and Structural Defects Favor Magnetic Hyperthermia Performance of Iron Oxide Nanocubes into Intracellular Environment. *Nano Lett.* **2018**, *18* (11), 6856–6866. https://doi.org/10.1021/acs.nanolett.8b02722.

(54) Walter, A.; Billotey, C.; Garofalo, A.; Ulhaq-Bouillet, C.; Lefèvre, C.; Taleb, J.; Laurent, S.; Vander Elst, L.; Muller, R. N.; Lartigue, L.; et al. Mastering the Shape and Composition of Dendronized Iron Oxide Nanoparticles To Tailor Magnetic Resonance Imaging and Hyperthermia. *Chem. Mater.* **2014**, *26* (18), 5252–5264. https://doi.org/10.1021/cm5019025.

(55) Wetterskog, E.; Tai, C.-W.; Grins, J.; Bergström, L.; Salazar-Alvarez, G. Anomalous Magnetic Properties of Nanoparticles Arising from Defect Structures: Topotaxial Oxidation of Fe $_{1-x}$ O|Fe $_{3-\delta}$ O $_4$ Core|Shell Nanocubes to Single-Phase Particles. *ACS Nano* **2013**, *7* (8), 7132–7144. https://doi.org/10.1021/nn402487q.

(56) Gerber, O.; Pichon, B. P.; Ulhaq, C.; Grenèche, J.-M.; Lefevre, C.; Florea, I.; Ersen, O.; Begin, D.; Lemonnier, S.; Barraud, E.; et al. Low Oxidation State and Enhanced Magnetic Properties Induced by Raspberry Shaped Nanostructures of Iron Oxide. *J. Phys. Chem. C* **2015**, *119* (43), 24665–24673. https://doi.org/10.1021/acs.jpcc.5b08164.

(57) Daou, T. J.; Pourroy, G.; Greneche, J. M.; Bertin, A.; Felder-Flesch, D.; Begin-Colin, S. Water Soluble Dendronized Iron Oxide Nanoparticles. *Dalton Trans* **2009**, No. 23, 4442–4449. https://doi.org/10.1039/b823187g.

(58) Mitra, A.; Mohapatra, J.; Meena, S. S.; Tomy, C. V.; Aslam, M. Verwey Transition in Ultrasmall-Sized Octahedral Fe3O4 Nanoparticles. *J. Phys. Chem. C* **2014**, *118* (33), 19356–19362. https://doi.org/10.1021/jp501652e.

(59) Özdemir, Ö.; Dunlop, D. J.; Berquó, T. S. Morin Transition in Hematite: Size Dependence and Thermal Hysteresis. *Geochem. Geophys. Geosyst.* **2008**, *9* (10), Q10Z01. https://doi.org/10.1029/2008GC002110.

(60) Bødker, F.; Mørup, S. Size Dependence of the Properties of Hematite Nanoparticles. *Europhys. Lett.* **52** (2), 217–223. https://doi.org/10.1209/epl/i2000-00426-2.

(61) Ortega, D.; Kuznetsov, M. V.; Morozov, Y. G.; Belousova, O. V.; Parkin, I. P. Thermal Relaxation and Collective Dynamics of Interacting Aerosol-Generated Hexagonal NiFe2O4 Nanoparticles. *Phys. Chem. Chem. Phys.* **2013**, *15* (48), 20830–20838. https://doi.org/10.1039/C3CP53981D.

(62) Alves, T. M. de L.; Amorim, B. F.; Torres, M. A. M.; Bezerra, C. G.; Medeiros, S. N. de; Gastelois, P. L.; Outon, L. E. F.; Macedo, W. A. de A. Wasp-Waisted Behavior in Magnetic Hysteresis Curves of CoFe2O4 Nanopowder at a Low Temperature: Experimental Evidence and Theoretical Approach. *RSC Adv.* **2017**, *7* (36), 22187–22196. https://doi.org/10.1039/C6RA28727A.

(63) Bødker, F.; Hansen, M. F.; Koch, C. B.; Lefmann, K.; Mørup, S. Magnetic Properties of Hematite Nanoparticles. *Phys. Rev. B* **2000**, *61* (10), 6826–6838. https://doi.org/10.1103/PhysRevB.61.6826.

(64) Kachkachi, H.; Dimian, M. Hysteretic Properties of a Magnetic Particle with Strong Surface Anisotropy. *Phys. Rev. B* **2002**, *66* (17), 174419. https://doi.org/10.1103/PhysRevB.66.174419.

(65) Cabrera, D.; Lak, A.; Yoshida, T.; Materia, M. E.; Ortega, D.; Ludwig, F.; Guardia, P.; Sathya, A.; Pellegrino, T.; Teran, F. J. Unraveling Viscosity Effects on the Hysteresis Losses of Magnetic Nanocubes. *Nanoscale* **2017**, *9* (16), 5094–5101. https://doi.org/10.1039/c7nr00810d.

(66) Morales, I.; Costo, R.; Mille, N.; Da Silva, G. B.; Carrey, J.; Hernando, A.; De la Presa, P. High Frequency Hysteresis Losses on γ-Fe2O3 and Fe3O4: Susceptibility as a Magnetic Stamp for Chain Formation. *Nanomaterials* **2018**, *8* (12), 970. https://doi.org/10.3390/nano8120970.

(67) Demortière, A.; Panissod, P.; Pichon, B. P.; Pourroy, G.; Guillon, D.; Donnio, B.; Bégin-Colin, S. Size-Dependent Properties of Magnetic Iron Oxide Nanocrystals. *Nanoscale* **2011**, *3* (1), 225–232. https://doi.org/10.1039/C0NR00521E.

(68) Rastei, M. V.; Pierron-Bohnes, V.; Toulemon, D.; Bouillet, C.; Kákay, A.; Hertel, R.; Tetsi, E.; Begin-Colin, S.; Pichon, B. P. Defect-Driven Magnetization Configuration of Isolated Linear Assemblies of Iron Oxide Nanoparticles. *Advanced Functional Materials* **2019**, *29* (45), 1903927. https://doi.org/10.1002/adfm.201903927.

(69) Roch, A.; Gillis, P.; Ouakssim, A.; Muller, R. N. Proton Magnetic Relaxation in Superparamagnetic Aqueous Colloids: A New Tool for the Investigation of Ferrite Crystal Anisotropy. *Journal of Magnetism and Magnetic Materials* **1999**, *201* (1), 77–79. https://doi.org/10.1016/S0304-8853(99)00078-5.

(70) Hergt, R.; Dutz, S. Magnetic Particle Hyperthermia—Biophysical Limitations of a Visionary Tumour Therapy. *Journal of Magnetism and Magnetic Materials* **2007**, *311* (1), 187–192. https://doi.org/10.1016/j.jmmm.2006.10.1156.

(71) Nielsen, S. B.; Wilhelm, K.; Vad, B.; Schleucher, J.; Morozova-Roche, L. A.; Otzen, D. The Interaction of Equine Lysozyme:Oleic Acid Complexes with Lipid Membranes Suggests a Cargo Off-Loading Mechanism. *Journal of Molecular Biology* 398 (2), 351–361.

(72) Lu, C.-W.; Hung, Y.; Hsiao, J.-K.; Yao, M.; Chung, T.-H.; Lin, Y.-S.; Wu, S.-H.; Hsu, S.-C.; Liu, H.-M.; Mou, C.-Y.; et al. Bifunctional Magnetic Silica Nanoparticles for Highly Efficient Human Stem Cell Labeling. *Nano Lett.* **2007**, *7* (1), 149–154. https://doi.org/10.1021/nl0624263.

(73) Walter, A.; Garofalo, A.; Parat, A.; Martinez, H.; Felder-Flesch, D.; Bégin-Colin, S. Functionalization Strategies and Dendronization of Iron Oxide Nanoparticles. *Nanotechnology Reviews* **2015**, *4* (6), 581. https://doi.org/10.1515/ntrev-2015-0014.

(74) Walter, A.; Garofalo, A.; Parat, A.; Jouhannaud, J.; Pourroy, G.; Voirin, E.; Laurent, S.; Bonazza, P.; Taleb, J.; Billotey, C.; et al. Validation of a Dendron Concept to Tune Colloidal Stability, MRI Relaxivity and Bioelimination of Functional Nanoparticles. *J. Mater. Chem. B* **2015**, *3* (8), 1484–1494. https://doi.org/10.1039/C4TB01954G.

(75) Starsich, F. H. L.; Eberhardt, C.; Boss, A.; Hirt, A. M.; Pratsinis, S. E. Coercivity Determines Magnetic Particle Heating. *Advanced Healthcare Materials* **2018**, *7* (19), 1800287. https://doi.org/10.1002/adhm.201800287.

1
2
3
4
5
6
7
8
9
10
11
12
13
14
15
16
17
18
19
20
21
22
23
24
25
26
27
28
29
30
31
32
33
34
35
36
37
38
39
40
41
42
43
44
45
46
47
48
49
50
51
52
53
54
55
56
57
58
59
60

(76) Smolensky, E. D.; Park, H.-Y. E.; Zhou, Y.; Rolla, G. A.; Marjańska, M.; Botta, M.; Pierre, V. C. Scaling Laws at the Nanosize: The Effect of Particle Size and Shape on the Magnetism and Relaxivity of Iron Oxide Nanoparticle Contrast Agents. *Journal of Materials Chemistry B* **2013**, *1* (22), 2818. https://doi.org/10.1039/c3tb00369h.

(77) Lee, J.-H.; Huh, Y.-M.; Jun, Y.; Seo, J.; Jang, J.; Song, H.-T.; Kim, S.; Cho, E.-J.; Yoon, H.-G.; Suh, J.-S.; et al. Artificially Engineered Magnetic Nanoparticles for Ultra-Sensitive Molecular Imaging. *Nat Med* **2007**, *13* (1), 95–99. https://doi.org/10.1038/nm1467.

(78) Joshi, H. M.; Lin, Y. P.; Aslam, M.; Prasad, P. V.; Schultz-Sikma, E. A.; Edelman, R.; Meade, T.; Dravid, V. P. Effects of Shape and Size of Cobalt Ferrite Nanostructures on Their MRI Contrast and Thermal Activation. *J Phys Chem C Nanomater Interfaces* **2009**, 113 (41), 17761–17767. https://doi.org/10.1021/jp905776g.

(79) Lee, N.; Choi, Y.; Lee, Y.; Park, M.; Moon, W. K.; Choi, S. H.; Hyeon, T. Water-Dispersible Ferrimagnetic Iron Oxide Nanocubes with Extremely High r_2 Relaxivity for Highly Sensitive in Vivo MRI of Tumors. *Nano Letters* **2012**, *12* (6), 3127–3131. https://doi.org/10.1021/nl3010308.

(80) Zhou, Z.; Tian, R.; Wang, Z.; Yang, Z.; Liu, Y.; Liu, G.; Wang, R.; Gao, J.; Song, J.; Nie, L.; et al. Artificial Local Magnetic Field Inhomogeneity Enhances T_2 Relaxivity. *Nature Communications* **2017**, *8*, ncomms15468. https://doi.org/10.1038/ncomms15468.

(81) Dunlop, D. J.; Özdemir, Ö. *Rock Magnetism: Fundamentals and Frontiers*; Cambridge University Press, 2001.

.

Table of Contents
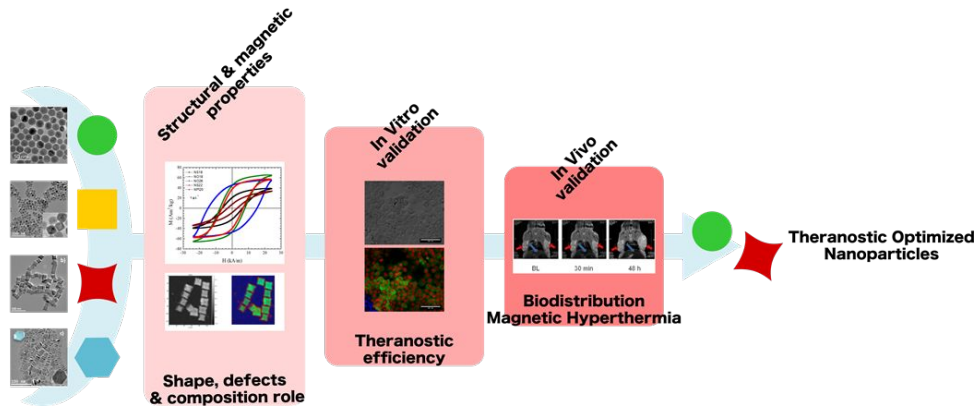
Theranosticity of nanoparticles provided by their shape, defects and dendron coating.